

Western  Graduate&PostdoctoralStudies

Western University
Scholarship@Western

Electronic Thesis and Dissertation Repository

12-14-2012 12:00 AM

Fast Absolute Quantification of In Vivo Water and Fat Content with Magnetic Resonance Imaging

Yifan Cui

The University of Western Ontario

Supervisor

Dr. Charles McKenzie

The University of Western Ontario

Graduate Program in Physics

A thesis submitted in partial fulfillment of the requirements for the degree in Master of Science

© Yifan Cui 2012

Follow this and additional works at: <https://ir.lib.uwo.ca/etd>



Part of the [Biological and Chemical Physics Commons](#), and the [Engineering Physics Commons](#)

Recommended Citation

Cui, Yifan, "Fast Absolute Quantification of In Vivo Water and Fat Content with Magnetic Resonance Imaging" (2012). *Electronic Thesis and Dissertation Repository*. 1040.

<https://ir.lib.uwo.ca/etd/1040>

This Dissertation/Thesis is brought to you for free and open access by Scholarship@Western. It has been accepted for inclusion in Electronic Thesis and Dissertation Repository by an authorized administrator of Scholarship@Western. For more information, please contact wlsadmin@uwo.ca.

Fast Absolute Quantification of *In Vivo* Water and Fat Content with Magnetic Resonance Imaging

Thesis format: Integrated Article

by

Yifan Cui

Graduate Program in Physics

A thesis submitted in partial fulfillment
of the requirements for the degree of
Master of Science

The School of Graduate and Postdoctoral Studies
The University of Western Ontario
London, Ontario, Canada

©Yifan Cui 2013

THE UNIVERSITY OF WESTERN ONTARIO
School of Graduate and Postdoctoral Studies

CERTIFICATE OF EXAMINATION

Supervisor

Examiners

Dr. Charles McKenzie

Dr. Eugene Wong

Supervisory Committee

Dr. Jerry Battista

Dr. Eugene Wong

Dr. Giles Santyr

Dr. Tamie Poepping

The thesis by

Yifan Cui

entitled:

**Fast Absolute Quantification of *In Vivo* Water and Fat Content with
Magnetic Resonance Imaging**

is accepted in partial fulfillment of the
requirements for the degree of
Master of Science

Date

Chair of the Thesis Examination Board

Abstract

Quantitative water fat imaging offers a non-invasive method for monitoring and staging diseases associated with changes in either water or fat content in tissue. In this work absolute water and fat mass density measurement with *in vivo* Magnetic Resonance Imaging (MRI) is demonstrated. T_1 independent, T_2^* corrected chemical shift based water-fat separated images are acquired. By placing a phantom with known mass density in the field of view for signal intensity calibration, absolute water or fat mass density can be computed, assuming the B_1^+ (transmit) and B_1^- (receive) fields can be measured. Phantom experiments with known water fat concentration were conducted to validate the feasibility of proposed method and *in vivo* data was collected from healthy volunteers. Results show good agreement with known values of *in vivo* water density. Each measurement was within one breath hold. Fast absolute quantification of water and fat with MRI is feasible in the abdomen.

Keywords

Magnetic Resonance Imaging (MRI), Water Fat Quantification, Absolute Quantification, B_1 Mapping, Coil Sensitivity

Co-Authorship Statement

Contribution of the work from others includes Dr. Trevor Wade in the flip angle mapping, Issac Yang and Curtis Wiens in phantom construction, and Abraam Soliman in IDEAL reconstruction. .

Acknowledgments

First, I would like to acknowledge my supervisor Dr. Charles McKenzie for his supervision and support during the entire master study here at the University of Western Ontario. This thesis would not have been possible without the guidance and the help of Dr. McKenzie. His acute and insights in research benefits me so much in developing the skills that will help me in my future career. I appreciate that Dr. McKenzie offered me the opportunity to work on an excellent project and be part of the McKenzie lab. I also would like to thank my advisory committee members Dr. Eugene Wong and Dr. Tamie Poepping for their constructive advice on my work. I would like to thank Curtis Wiens. He is a PhD student and always gave me a lot of help whenever I encountered any problem. I also would like to thank Issac Yang, who gave me a lot of support when we were working together. Many thanks to Dr. Trevor Wade, who is a postdoc in McKenzie lab and provided valuable help to me. Lastly, I would like to thank Abraam Soliman, Lanette Friesen-Waldner, Samantha Flood and the entire lab for their support and help. I would like to point out that these are not forgotten and I appreciate all of them. I would like to particularly thank them in helping me to make it fun to work and all the memories for over the last two years.

Again, thank you all so much for your help and support,

Yifan

Table of Contents

CERTIFICATE OF EXAMINATION	ii
Abstract.....	iii
Co-Authorship Statement.....	iv
Acknowledgments.....	v
Table of Contents	vi
List of Figures	ix
Chapter 1	1
1 Introduction	1
1.1 Non-Alcoholic Fatty Liver Disease (NAFLD)	2
1.2 MRI Physics.....	6
1.2.1 Spin, Properties of Spin	6
1.2.2 RF Excitation, Bloch Equations, T_1 and T_2 Relaxation	10
1.2.3 Faraday Induction and Signal from Precession	15
1.2.4 Slice Selection.....	16
1.2.5 Frequency Encoding	18
1.2.6 Phase Encoding.....	19
1.2.7 3D Spatial Encoding	20
1.3 Fat Water Separation.....	23
1.3.1 Two Point Dixon Method	24
1.3.2 Three Point Dixon Method	27
1.3.3 Multi-peak T_2^* Corrected IDEAL.....	31
1.3.4 Multi-peak T_2^* IDEAL Fat Fraction	33
1.4 Coil Sensitivity.....	34
1.5 Flip Angle Mapping.....	37

1.5.1	Overview on Flip Angle Mapping	37
1.5.2	Double Angle Method.....	38
1.5.3	Look-Locker Sequence	39
1.5.4	Flip Angle Measurement with the Double Angle Look-Locker Sequence	40
Chapter 2	42
2	Absolute Water and Fat Quantification Using MRI	42
2.1	Introduction.....	43
2.2	Theory	46
2.2.1	B_1^+ Transmit Field Inhomogeneity Factor $k_{B_1^+}^{vc}$	47
2.2.2	B_1^- Phased Array Receive Field Sensitivity Profile c	48
2.2.3	Image Reconstruction	50
2.3	Methods.....	53
2.3.1	Phantom Experiments	53
2.3.2	In Vivo Experiments	53
2.4	Result	54
2.4.1	Phantom Experiments	54
2.4.2	In Vivo Experiments.....	57
2.5	Discussion.....	59
2.6	Conclusion	61
Chapter 3	62
3	Summary and Future Work.....	62
3.1	Summary	63
3.2	Future work.....	65
3.2.1	T_1 Correction	65
3.2.2	Flip Angle Map Correction on Volume Coil	66

3.2.3	Temperature Correction	66
3.2.4	Cardiac Application	67
3.2.5	Application in Hyperpolarized Imaging	68
3.3	Conclusion	69
	References.....	70
	Curriculum Vitae	76

List of Figures

Figure 1-1: Abdominal opposed phase MRI image of a patient with NAFLD. Visible non-uniform distribution of fat content shows the possible sampling error when performing conventional liver biopsy. Arrow ‘a’ points to normal tissue, while arrow ‘b’ points to a region of steatosis. Steatotic regions appear dark because the water and fat signals have opposite phase and therefore the signal from fat partly cancels out the signal from water. 4

Figure 1-2: For a collection of a large number of protons at thermal equilibrium, individual magnetization orients randomly, resulting in zero net magnetization. 8

Figure 1-3: In the presence of a B_0 external magnetic field, there are only two orientations for protons, parallel or anti-parallel to B_0 . The number of protons in those two states is different, according to the Boltzmann distribution, and forms the net longitudinal magnetization M_0 . Where ω_0 is the Larmor angular frequency in rad/s, B_0 is the field strength in Tesla (T) that the protons are experiencing, and γ is the gyromagnetic ratio, a constant for each particular nucleus in $rad \cdot s^{-1} \cdot T^{-1}$ 8

Figure 1-4: In the rotating reference frame, the can be tipped off the z axis by any desired degree by manipulating the strength or duration of the \vec{B}_1 field. 11

Figure 1-5: Demonstration of slice thickness. With the same bandwidth, different gradient results in different slice thickness. 17

Figure 1-6: A sequence diagram for a 3D coverage and data collection. Gradients are applied along read out direction and y z phase encoding directions. The role each gradient plays is indicated in the figure. 22

Figure 1-7: Two point Dixon method. Two images are acquired at different TEs when water and fat signal are in-phase and out-of-phase. By adding (a) and subtracting (b) these two images, water and fat images can be generated. This assumes a perfectly uniform B_0 magnetic field..... 25

Figure 1-8: With non-uniform B_0 field, additional phase will accumulate. Simply adding and subtracting is not going to generate water and fat separated images..... 26

Figure 1-9: Three-point Dixon method. Images are collected at three different echoes, with the relative phases between water and fat are $(-\pi, 0, \pi)$	29
Figure 1-10: A representative spectrum collected in knee subcutaneous fat at 3T showing multi-peak pattern. Six peaks can be recognized and their relative chemical shift and amplitude can be calculated (13).	30
Figure 1-11: Conventional Look-Locker sequence. An image is created for each α sampling pulse, and t_d and t_r are the time delays before and after the α -pulse train, τ is the repetition time.	39
Figure 2-1: Flow chart of image acquisition and reconstruction. Flip angle maps were acquired for both $k_{B_1^+}^{vc}$ and c correction. The volume coil image was first corrected for B_1^- using flip angle map as an approximation. Images from phased array were divided by the volume coil image to generate the phased array surface coil sensitivity maps. With these maps, coil by coil images were combined. Then those corrected images were run through the IDEAL reconstruction to get water and fat separated images with arbitrary units. By calibrating with a phantom with known proton density, water and fat mass maps were generated.	51
Figure 2-2: Phantom result. Top two images are water and fat mass density map before all the correction, bottom two images are water and fat mass density map.....	56
Figure 2-3: Calibrated water and fat mass density in each vial against the known water and fat mass density. Linear regression shows slope of 0.99, and intercept of 0.002 g/ml and a correlation coefficient of $R^2 = 0.99$	56
Figure 2-4: <i>In vivo</i> images of a volunteer's calves. (The object between the calves is a pure fat mass density reference.) The corrected water and fat images are noticeably more uniform than the uncorrected images, particularly at the periphery. The circle in the corrected water image indicates the ROI in which muscle density was measured.	58
Figure 2-5: <i>In vivo</i> images of a volunteer's liver. (The object beside the abdomen is a bottle of water as mass density reference.) The corrected water and fat images are noticeably more	

uniform than the uncorrected images across the liver. The circle on the corrected water image indicated the liver density measurement location. 58

Chapter 1

1 Introduction

In this thesis, a new method for fast absolute quantification of water and fat content *in vivo* is introduced. A series of corrections were combined to correct Magnetic Imaging Resonance (MRI) images so that absolute water and fat mass density maps can be generated. Each measurement is under one breath hold. In this chapter, a brief introduction to background of each of these correction methods is provided to help explain the experimental method for absolute water and fat quantification.

1.1 Non-Alcoholic Fatty Liver Disease (NAFLD)

Nonalcoholic fatty liver disease (NAFLD), which is characterized by fat accumulation in the liver, is commonly seen in the clinic. NAFLD affects 10-24% of the population worldwide (1). NAFLD is considered to be the most common liver disease in the western world, regardless of racial and ethnic group. In the United States, NAFLD affects over 75% of the obese individuals (2,3). Most alarmingly, 2.6% of children are affected by NAFLD, and this portion includes 22.5-52.8% of obese children (4). Nonalcoholic steatohepatitis (NASH), which is the more advanced form of NAFLD, is estimated to affect 20% of the obese population (3). NAFLD can be found in all age groups and the prevalence appears to increase with age (3).

NAFLD has hepatic pathology similar to liver diseases induced by alcohol, but it develops in individuals who have no history of excessive alcohol intake. NAFLD has a wide spectrum of liver damage, progressing from hepatic steatosis (accumulation of fat in liver cells), through steatohepatitis (NASH, accompanied by liver cell injury and death) to cirrhosis and consequent liver-related morbidity and mortality (5). Though macro-vesicles and micro-vesicles of fat accumulate in the hepatocytes, hepatic steatosis alone does not tend to cause hepatic inflammation or liver cell death. Steatohepatitis is considered the middle stage of liver damage. Focal hepatic inflammation occurs and the hepatocytes start to die with steatohepatitis. Cirrhosis sits on the end of the spectrum. It is scarring of the liver and poor liver function. Scar tissue replaces normal parenchyma, blocking the portal flow of blood through the organ. In this stage, architectural distortion has developed, but hepatic steatosis has often disappeared (1).

NAFLD leads to NASH, which can be fatal. If caught early, NAFLD can be reversed before irreversible liver damage due to NASH occurs. Thus early detection and diagnosis of NAFLD is necessary.

Liver biopsy is currently considered the gold standard for the diagnosis of NAFLD. A piece of hepatic tissue is taken out of the patient and examined in the pathology lab in order to stage the disease progress. Biopsy is an invasive method where a needle is inserted into the organ, and a tiny small portion of tissue is taken out and then examined in a laboratory. This procedure is painful and has some inherent risks. Life-threatening situations and prolonged hospitalization is reported in 3 out of 1000 cases, and death is reported in 3 out of 10000 cases (6,7). Furthermore, the sample that is only 1/50000 of the entire liver is used to represent the liver. Several studies have been published showing sampling variability when more than one sample is obtained (8). Studies show that the possibility of finding fatty cells on a second liver biopsy when the first biopsy showed nothing is as high as 22 % (8). As is shown in figure 1-1, the inhomogeneous distribution of steatosis makes sampling variability inevitable and unreliable.

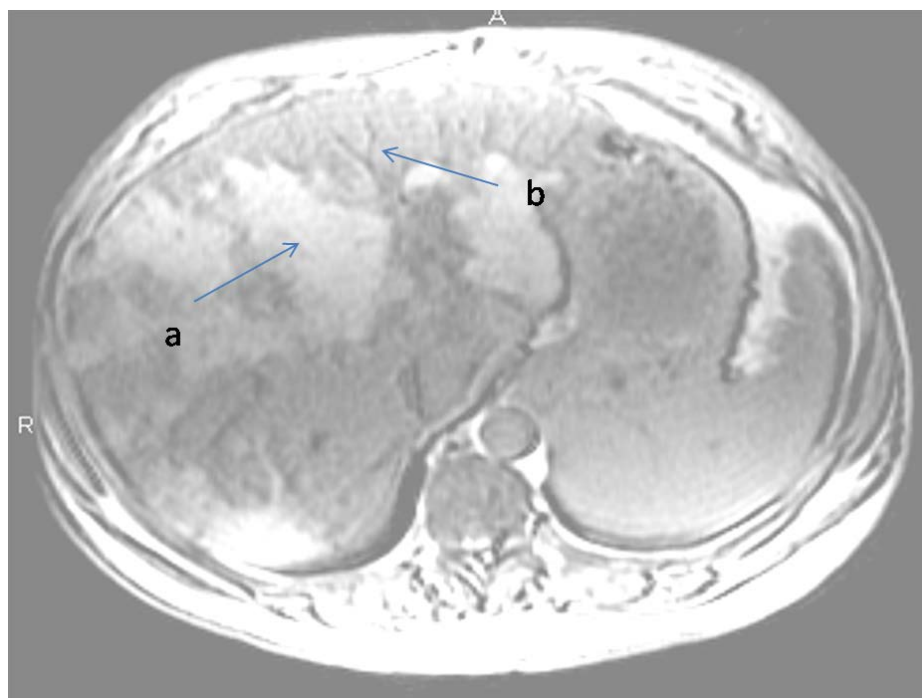


Figure 1-1: Abdominal opposed phase MRI image of a patient with NAFLD. Visible non-uniform distribution of fat content shows the possible sampling error when performing conventional liver biopsy. Arrow 'a' points to normal tissue, while arrow 'b' points to a region of steatosis. Steatotic regions appear dark because the water and fat signals have opposite phase and therefore the signal from fat partly cancels out the signal from water.

Thus the sampling error might lead to misdiagnosis and is not appropriate for evaluating treatment response. In longitudinal monitoring, samples are supposed to be taken from the same location. However even the biopsies were obtained by experienced doctors, locations tend to vary from time to time. In this case, the non-uniform fat distributions may lead to misdiagnoses.

A non-invasive method that can accurately detect and quantify liver steatosis is an unmet need for the diagnosis of NAFLD. Magnetic Resonance Imaging (MRI) techniques have been shown to be a promising diagnostic method to replace the current gold standard liver biopsy. A recent study has shown that chemical shift based MRI measurement of fat correlates well with Magnetic Resonance Spectroscopy (MRS) (9), while MRS result has already been demonstrated to have excellent correlation with the gold standard biopsy measurement of liver fat (10).

MRI has many advantages over biopsy in measuring fat content in the liver. First it is a non-invasive method so that patients can be examined much more frequently. This could make it possible for closer monitoring of the disease progression. In addition, doctors would be able to get an accurate measurement of the spatial distribution of fat content over the entire liver, which is crucial to avoid sampling errors. Furthermore, MRI would significantly lower the risk of complications compared with liver biopsy, thus leading to a safe painless test.

1.2 MRI Physics

1.2.1 Spin, Properties of Spin

All atoms have the nuclei-electron structure. Spin (or formally called spin angular momentum), which is one of the intrinsic properties of nuclei, can be probed with an external magnetic field using a technique named nuclear magnetic resonance (NMR).

Nuclei with spin can be considered as a charged ball rotating about an axis with constant angular velocity. Spin is quantized to certain discrete values, and the number of spin values, I , is found to have limited numbers in nature. Among several different nuclei that can be used in human imaging, nucleus of ^1H atom (commonly referred to as proton) is the natural choice for most applications. Tissue in the body is mostly composed of water and fat. Water and fat contains hydrogen atoms, the nucleus of which provides NMR signal.

Though an accurate description of the magnetic resonance (MR) phenomenon requires quantum mechanics, a classical model can be used to describe MR experiments. The classical model ultimately gives the same result as the quantum mechanical model. A spinning proton will induce a magnetic field known as a magnetic moment that is oriented parallel to the axis of rotation. The concept of magnetic moment is fundamental to MR. Just like a bar magnet, the magnetic moment can be described as a vector with magnitude and a certain direction.

In the absence of an external magnetic field, spins have their orientation randomly distributed. The vector sum of a bulk of spins generates zero net magnetic field (Figure 1-2). However, when an external magnetic field B_0 is applied, the protons start to precess

about the direction of magnetic field. The frequency of precession is proportional to the strength of B_0 , which can be described by the Larmor equation:

$$\omega_0 = \gamma B_0. \quad \text{Eq. 1-1}$$

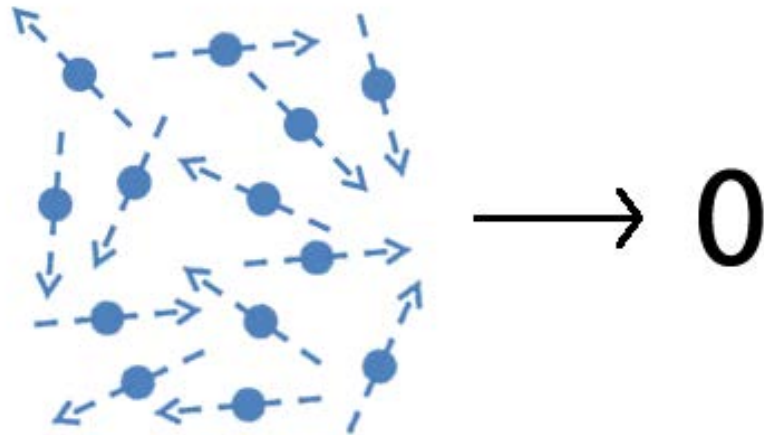


Figure 1-2: For a collection of a large number of protons at thermal equilibrium, individual magnetization orients randomly, resulting in zero net magnetization.

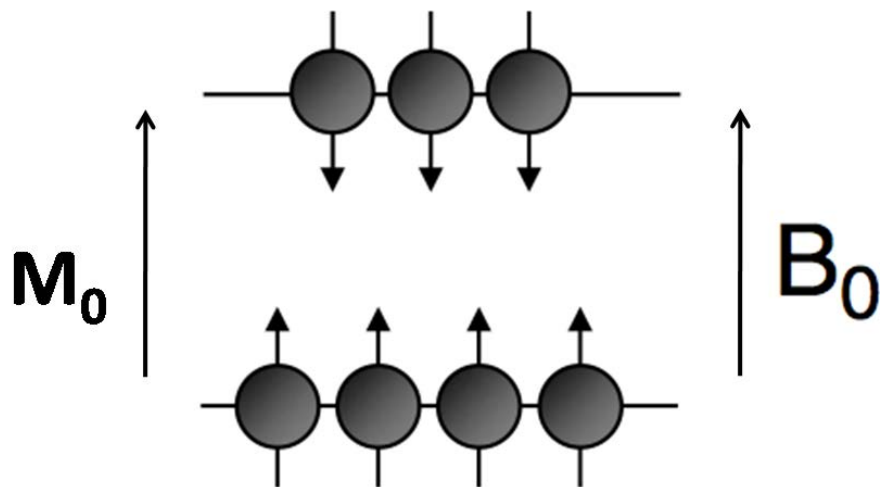


Figure 1-3: In the presence of a B_0 external magnetic field, there are only two orientations for protons, parallel or anti-parallel to B_0 . The number of protons in those two states is different, according to the Boltzmann distribution, and forms the net longitudinal magnetization M_0 .

Where ω_0 is the Larmor angular frequency in rad/s, B_0 is the field strength in Tesla (T) that the protons are experiencing, and γ is the gyromagnetic ratio, a constant for each particular nucleus in $rad \cdot s^{-1} \cdot T^{-1}$.

Since each individual proton precesses about the B_0 field independently, if we consider the vector sum of a collection of many protons, the transverse components of the individual spins will still be randomly oriented. Thus, the net transverse magnetization is zero. However, the z (longitudinal) component parallel to B_0 is different. For protons, there are only two possible values for the z component: parallel or anti-parallel to B_0 (often referred to as spin up and down). According to the Boltzmann distribution, the number of protons in those two states is different, and those numbers of protons up and down obeys the following:

$$\frac{N_{down}}{N_{up}} = e^{-\Delta E/kT}, \quad \text{Eq. 1-2}$$

where k is Boltzmann's constant, N_{up} and N_{down} are the number of protons aligning and anti-aligning with the B_0 field, ΔE is the energy different between two different energy levels, T is the temperature in Kelvin temperature scale. When tissue with large amounts of protons is put in an external magnetic field, the tissue will be polarized with a net magnetization \vec{M}_0 , which is visualized in Figure 1-3. At thermal equilibrium, \vec{M}_0 has the same direction as B_0 and the magnitude of \vec{M}_0 does not change with time. For the rest of this section, we are going to talk about behavior of \vec{M}_0 and how to measure it.

1.2.2 RF Excitation, Bloch Equations, T_1 and T_2 Relaxation

As discussed above, \vec{M}_0 will precess in an external magnetic field. Thus, we can use another field to manipulate \vec{M}_0 . The magnetic field used is often derived from a narrow bandwidth, radio-frequency pulse (RF pulse). If the frequency of the RF pulse matches the resonant frequency (Larmor frequency) of the protons, \vec{M}_0 , and the effective field (referred to as B_1) stays stationary in a rotating reference frame, which is rotating about the z direction with Larmor frequency. In the rotating reference frame, \vec{M}_0 will precess about the B_1 field. The duration of the B_1 field can be manipulated so that \vec{M}_0 is tipped off the longitudinal axis by any desired degree, see Figure 1-4.

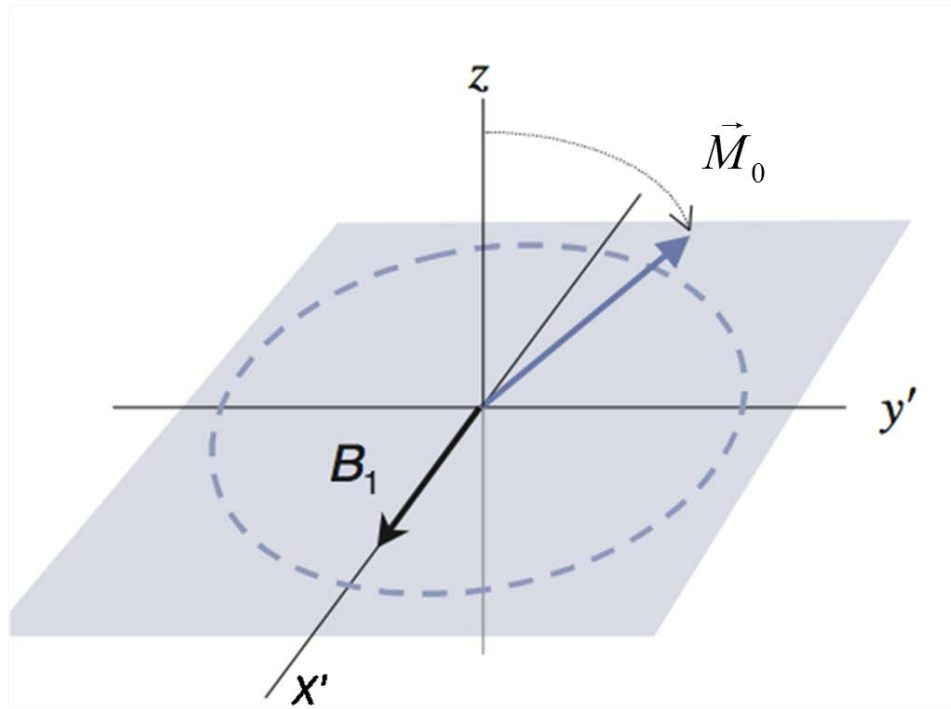


Figure 1-4: In the rotating reference frame, the can be tipped off the z axis by any desired degree by manipulating the strength or duration of the \vec{B}_1 field.

After the RF pulse, the magnetization \vec{M}_0 is no longer along the z longitudinal axis. The magnetization then can be decomposed into two components: M_z and \vec{M}_{xy} . After the \vec{B}_1 field is turned off, the transverse component \vec{M}_{xy} , which is perpendicular to the \vec{B}_0 field, starts to precess about \vec{B}_0 . This precession induces a voltage that can be detected by a coil of wire. The induced voltage is actually the signal that we use to get our image, and it is known as free induction decay (FID).

1.2.2.1 Bloch Equation

The differential equations of longitudinal and transverse magnetization can be combined into vector form as follows:

$$\frac{d\vec{M}}{dt} = \gamma \vec{M} \times \vec{B}_0 + \frac{1}{T_1} (M_0 - M_z) \hat{z} - \frac{1}{T_2} \vec{M}_{xy}, \quad \text{Eq. 1-3}$$

where \vec{M} is the net magnetization, M_z is its longitudinal component, \vec{M}_{xy} is its transverse component, \vec{B}_0 is the external magnetic field, M_0 is the magnitude of net magnetization at thermal equilibrium, T_1 and T_2 are constant values.

This equation is known as the Bloch equation; it describes the behavior of the magnetization in an external magnetic field $\vec{B}_0 = B_0 \hat{z}$. This equation can be separated into three component equations:

$$\frac{dM_z}{dt} = \frac{M_0 - M_z}{T_1}, \quad \text{Eq. 1-4}$$

$$\frac{dM_x}{dt} = \omega_0 M_y - \frac{M_x}{T_2}, \quad \text{Eq. 1-5}$$

$$\frac{dM_y}{dt} = \omega_0 M_x - \frac{M_y}{T_2}. \quad \text{Eq. 1-6}$$

Solutions of each component can be found by solving these equations as:

$$M_x(t) = e^{-t/T_2} (M_x(0) \cos \omega_0 t + M_y(0) \sin \omega_0 t), \quad \text{Eq. 1-7}$$

$$M_y(t) = e^{-t/T_2} (M_y(0) \cos \omega_0 t - M_x(0) \sin \omega_0 t), \quad \text{Eq. 1-8}$$

$$M_z(t) = M_z(0) e^{-t/T_1} + M_0 (1 - e^{-t/T_1}). \quad \text{Eq. 1-9}$$

From this solution set, the transverse magnetization \vec{M}_{xy} is rotating in x - y plane while decaying away. The circular motion will induce a current in the detecting coil, which is the signal we use to get the image.

1.2.2.2 T_1 and T_2 Relaxation

While \vec{M} is precessing, the magnitude of \vec{M}_{xy} decays away exponentially. At the same time, the longitudinal magnetization M_z starts to recover to its original value. These changes in magnetization are known as relaxation. This is a time dependent process, which can be characterized by the relaxation times T_1 and T_2 .

The relaxation time T_1 represents the rate of change of the longitudinal magnetization (M_z). Both theoretical and experimental results show that the rate of the growth of

longitudinal magnetization, $dM_z(t)/dt$, is proportional to the difference $M_0 - M_z$. The

rate is just inverse of T_1 and determined by experiments. The equation of M_z can be written as:

$$\frac{dM_z}{dt} = \frac{1}{T_1}(M_0 - M_z), \quad \text{Eq. 1-10}$$

where T_1 is the 'spin-lattice relaxation time' and the direction of the external B_0 field is along the z axis. The solution to this equation is:

$$M_z(t) = M_z(t_0)e^{-(t-t_0)/T_1} + M_0(1 - e^{-(t-t_0)/T_1}), \quad \text{Eq. 1-11}$$

where $M_z(t_0)$ is the initial z component of magnetization at time point t_0 .

The actual external field that each individual spin experiences is actually a vector sum of the external field B_0 and the magnetic field of neighboring spins. Thus, each spin experiences a slightly different local field, which leads to a slightly different resonance frequency. This leads to the direction of the transvers magnetization of each spin tending to change relative to the other spins with time. Since the spins are pointing in different directions, the vector sum of their signals results in reducing the overall magnitude of \vec{M}_{xy} . This is referred to as dephasing. The relaxation T_2 represents the rate of decay of the transverse magnetization \vec{M}_{xy} . T_2 is an experimental parameter. The equation that describes transverse magnetization is:

$$\frac{d\vec{M}_{xy}}{dt} = \gamma \vec{M}_{xy} \times \vec{B}_0 - \frac{1}{T_2} \vec{M}_{xy}. \quad \text{Eq. 1-12}$$

In the rotational reference frame, it is easier to see its decay form:

$$\left(\frac{d\vec{M}_{xy}}{dt}\right)' = -\frac{1}{T_2}\vec{M}_{xy}. \quad \text{Eq. 1-13}$$

In practice, there are some other factors, such as inhomogeneous B_0 field or iron overload in liver, that would contribute to the decay of transverse magnetization, such as the. If we use T_2' to characterize those extra dephasing factors, a new relaxation time constant T_2^* can be defined as follows:

$$\frac{1}{T_2^*} = \frac{1}{T_2} + \frac{1}{T_2'}. \quad \text{Eq. 1-14}$$

In gradient echo, those extra dephasing will not be reverted, and the decay of transverse magnetization is characterized by T_2^* . Thus T_2^* is especially important in gradient echo experiments.

1.2.3 Faraday Induction and Signal from Precession

According to Faraday's law, a change of magnetic flux (Φ) due to the precession of transverse magnetization \vec{M}_{xy} will induce an electromotive force (EMF) in the detection coil:

$$emf = -\frac{d\Phi}{dt}, \quad \text{Eq. 1-15}$$

where Φ is the flux through the coil:

$$\Phi = \int_{coilarea} \vec{B} \cdot d\vec{S}, \quad \text{Eq. 1-16}$$

where $d\vec{S}$ is the vector area element, the direction of which is perpendicular to its surface.

Since the magnetization of the protons in our sample is precessing at the Larmor frequency, the current induced in the coil will also be oscillating at that frequency.

1.2.4 Slice Selection

In order to excite a particular region of interest in the sample, a frequency selective RF pulse is applied with a magnetic field gradient known as slice-selection gradient, G_{ss} (mT/m). The slice orientation depends on the gradient direction, and the amplitude of the gradient along with the frequency of the RF pulse determines the thickness and location of the slice. The slice selective pulse usually has a central frequency ω_0 and a narrow frequency range or bandwidth $\Delta\omega_{ss}$. With the presence of the gradient, the central frequency determines the location of the slice, while the bandwidth determines its thickness:

$$\Delta\omega_{ss} = \frac{\gamma}{2\pi} (G_{ss} \times thickness) . \quad \text{Eq. 1-17}$$

Typically the bandwidth of the RF pulse is fixed and the slice thickness is adjusted by changing the strength of gradient (Figure 1-5).

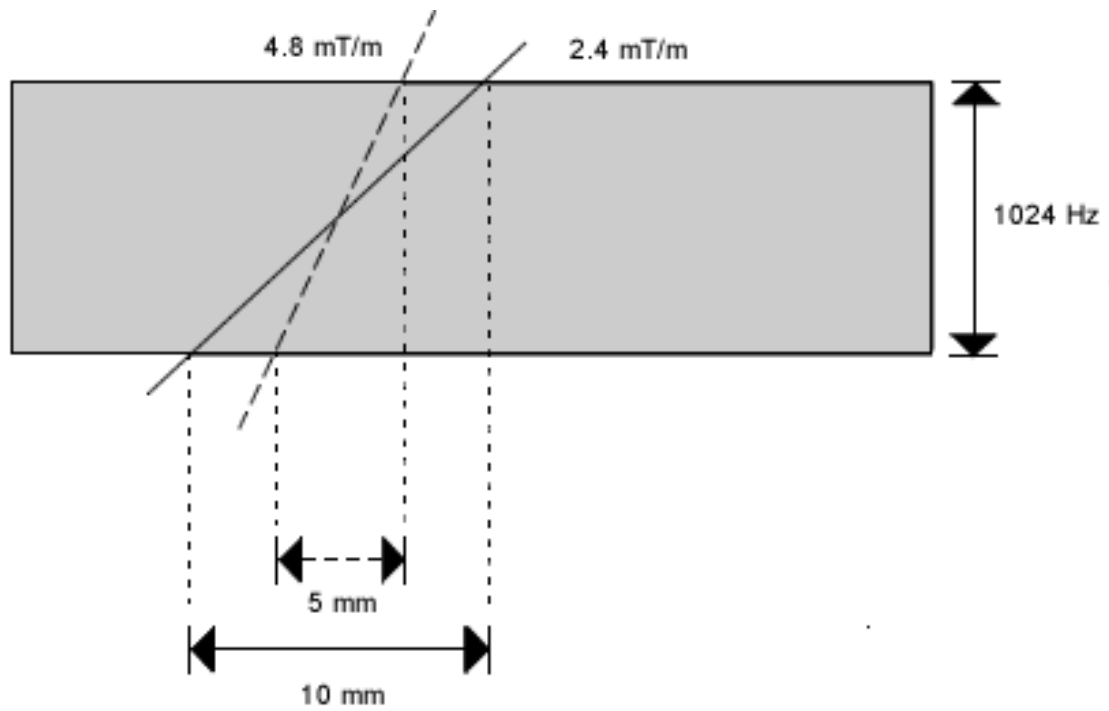


Figure 1-5: Demonstration of slice thickness. With the same bandwidth, different gradient results in different slice thickness.

1.2.5 Frequency Encoding

If a magnetic field ($B' = xG$), which is linearly varying along the x axis, is added to the static magnetic field B_0 , then the z component of the field is going to be:

$$B_0(x) = B_0 + xG . \quad \text{Eq. 1-18}$$

Thus Larmor equation will then be:

$$\omega(x) = \omega_0 + x \cdot \gamma G . \quad \text{Eq. 1-19}$$

Extra phase accumulated due to the presence of gradient can be calculated as:

$$\phi_G(x, t) = -\int_0^t dt' \omega_G(x) = -\gamma x \int_0^t dt' G . \quad \text{Eq. 1-20}$$

The signal at time t, after demodulating frequency $\Omega = \omega_0$, is given by:

$$s(t) = \int dx \rho(x) e^{i\phi_G(x, t)} . \quad \text{Eq. 1-21}$$

where the phase, after demodulation is determined by gradient field.

If the time dependence term is implicitly included in spatial frequency k with:

$$k_x = \frac{\gamma}{2\pi} \int_0^t G(t') dt' . \quad \text{Eq. 1-22}$$

the signal at time t can be expressed as:

$$s(k_x) = \int dx \rho(x) e^{-i2\pi x k_x} . \quad \text{Eq. 1-23}$$

This means if a gradient along certain direction is applied during the signal acquisition, the proton density along that direction can be recovered by simply taking the inverse Fourier transform of the signal:

$$\rho(x) = \int dk_x \rho(k_x) e^{+i2\pi x k_x} . \quad \text{Eq. 1-24}$$

In MRI, this is always referred to as frequency encoding and the direction is referred to as the readout direction.

1.2.6 Phase Encoding

Similarly as frequency encoding, if a magnetic field ($B' = yG$), which is linearly varying along the y axis, is added to the static magnetic field B_0 , then the z component of the field is going to be:

$$B_0(y) = B_0 + yG . \quad \text{Eq. 1-25}$$

Thus Larmor equation will then be:

$$\omega(y) = \omega_0 + y \cdot \gamma G . \quad \text{Eq. 1-26}$$

If the phase encoding gradient is turned on for a short period of time Δt and then turned off, extra phase accumulated due to the presence of this momentary gradient can be calculated as:

$$\phi_G(y) = -\Delta t \cdot \omega_G(y) = -\gamma y \cdot G \Delta t . \quad \text{Eq. 1-27}$$

If the time dependence term is implicitly included in spatial frequency k with:

$$k_y = \frac{\gamma}{2\pi} \Delta t \cdot G , \quad \text{Eq. 1-28}$$

the signal along phase encoding direction in k space can be expressed as:

$$s(k_y) = \int dy \rho(y) e^{-i2\pi y k_y} . \quad \text{Eq. 1-29}$$

This means if a phase encoding gradient increment is added each time when we acquire a line in k space along frequency encoding direction, the proton density along the phase encoding direction can be recovered by simply taking the inverse Fourier transform of the signal:

$$\rho(y) = \int dk_y s(k_y) e^{+i2\pi y k_y} . \quad \text{Eq. 1-30}$$

1.2.7 3D Spatial Encoding

Consider an extension of the one dimensional imaging equation to the three dimensional case. With three orthogonal gradients the signal from a single RF excitation can be expressed as a 3D Fourier transformation:

$$s(k_x, k_y, k_z) = \iiint dx dy dz \rho(x, y, z) e^{-i2\pi(k_x x + k_y y + k_z z)} , \quad \text{Eq. 1-31}$$

where the three implicitly time-dependent components are defined as

$$k_x = \frac{\gamma}{2\pi} \int_0^t G_x(t') dt' , \quad \text{Eq. 1-32}$$

$$k_y = \frac{\gamma}{2\pi} \int_0^t G_y(t') dt' , \quad \text{Eq. 1-33}$$

$$k_z = \frac{\gamma}{2\pi} \int_0^t G_z(t') dt' . \quad \text{Eq. 1-34}$$

If 3D k-space is sufficiently sampled, the reconstructed image by taking the inverse Fourier transform of the signal should be an accurate estimate of the physical density:

$$\hat{\rho}(\vec{r}) = \int d^3k \cdot s(\vec{k}) e^{i2\pi\vec{k}\cdot\vec{r}} . \quad \text{Eq. 1-35}$$

In the 3D experiment, a thicker slice is always excited and then phase encoded in the y and z directions. By convention, x direction is always the readout direction. A readout gradient is applied when signal is detected by the receiving coil. This gives a line along x axis in k-space. By momentarily adding gradient in y and z direction, we can move to a particular k_y and k_z position in k-space.

In the x direction (readout direction), sampling can be carried out by measuring signal with time interval Δt during continuous application of a gradient G_x . Thus in the k_x direction:

$$\Delta k_x = \gamma G_x \Delta t / 2\pi . \quad \text{Eq. 1-36}$$

However in k_y and k_z directions, gradients G_y and G_z are turned off during the data reading out, in order to keep each line parallel to the x direction. Before data is taken, the k_y and k_z position in each line is determined by applying G_y and G_z for short time τ_y and τ_z . The corresponding shifts in k-space are:

$$\Delta k_y = \gamma \Delta G_y \tau_y / 2\pi , \quad \text{Eq. 1-37}$$

$$\Delta k_z = \gamma \Delta G_z \tau_z / 2\pi , \quad \text{Eq. 1-38}$$

where the y and z axes are referred as phase encoding directions in a 3D imaging experiment. This is illustrated in the sequence diagram in Figure 1-6.

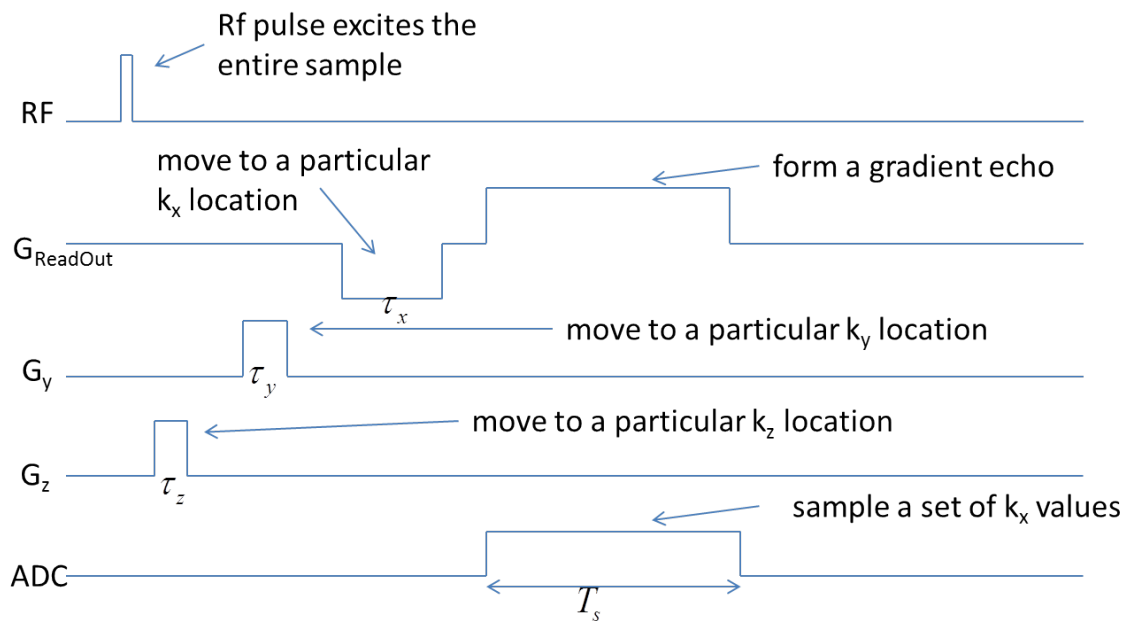


Figure 1-6: A sequence diagram for a 3D coverage and data collection. Gradients are applied along read out direction and y z phase encoding directions. The role each gradient plays is indicated in the figure.

1.3 Fat Water Separation

Even if a perfectly uniform external static field could be achieved, the local field experienced by each molecule can still be different. For instance, the local magnetic field experienced by a proton on water molecule is slightly different from that experienced by protons in a fat compound. Because of the structure of fat molecule, the magnetic field produced by surrounding electrons will affect the net magnetic field that protons are experiencing. The term chemical shift refers to the difference in the resonance frequency between two proton MR signals, expressed in parts per million of the resonance frequency of the static magnetic field B_0 . Chemical shift imaging is the process of imaging the different spatial distributions of the same nuclei that are resonating at different frequencies because of their different local environment (e.g. ^1H nuclei in water vs. fat molecules).

When a nonselective radiofrequency pulse is applied, protons in both water and fat molecules are excited. However, due to the chemical shift effect, protons in water precess faster than those in fat by approximately 3.5 parts per million (ppm). The difference between their precession frequencies Δf_{wf} is given by:

$$\Delta f_{wf} = f_w - f_f = -\sigma_{wf} \gamma B_0 / 2\pi, \quad \text{Eq. 1-39}$$

where the suffix w stands for water, f for fat, σ_{wf} is the chemical shift between fat and water expressed in ppm. The absolute difference in the resonant frequencies between the two species is about 224Hz at 1.5T, and 447Hz at 3.0T. There are many ways to image

fat and water separately, which are described as ‘selective excitation’, ‘T₁ nulling’ and using chemical shift to generate additional phase encoding information.

A variety of methods can be used to separate the signals from water and fat. Selective excitation uses a RF pulse with a specific bandwidth that selectively excites protons in fat (or water) molecules only. However, the downside of this method is that a perfectly homogeneous main magnetic field is required. In Short TI Inversion Recovery (STIR), after an inversion recovery preparation, signal is collected at the time point when the undesired fat magnetization has recovered to the point where it is crossing $M_z=0$, thus eliminating any fat signal. But this inversion recovery sequence requires long repetition time (TR) to allow the longitudinal signal to recover to M_0 before the next inversion pulse. For this reason, the acquisition time is rather long. Because of these reasons, chemical shift based imaging techniques described below are used in this thesis work for the separation of water and fat signals.

1.3.1 Two Point Dixon Method

If the precession frequencies of water and fat are taken as priori knowledge, the imaging scheme to separate those two species can be much simplified.

Assuming the tissue only consists of water and fat, the complex (real and imaginary) signal from a particular pixel can be expressed as:

$$s(TE) = \rho_w + \rho_f, \quad \text{Eq. 1-40}$$

where $s(TE)$ represents the complex signal obtained at echo time TE , ρ_w and ρ_f are the intensity of water and fat that we are interested in (11). If it is assumed that the static field

is homogeneous throughout the whole volume imaged, the phase accumulated in water and fat at echo time t' are:

$$\varphi_w(t') = -\gamma G_x x t' = -2\pi k_x x, \quad \text{Eq. 1-41}$$

$$\varphi_f(t') = -\gamma(G_x x + \Delta B_{wf})t' - \gamma \Delta B_{wf} TE = -2\pi k_x (x + \Delta B_{wf} / G_x) - \Delta\omega_{wf} TE. \quad \text{Eq. 1-42}$$

The additional accumulated phase in the fat signal can be used to separate the water and fat signals. Two complex signals are acquired with different TE s that make $\Delta\omega_{wf} TE$ equal

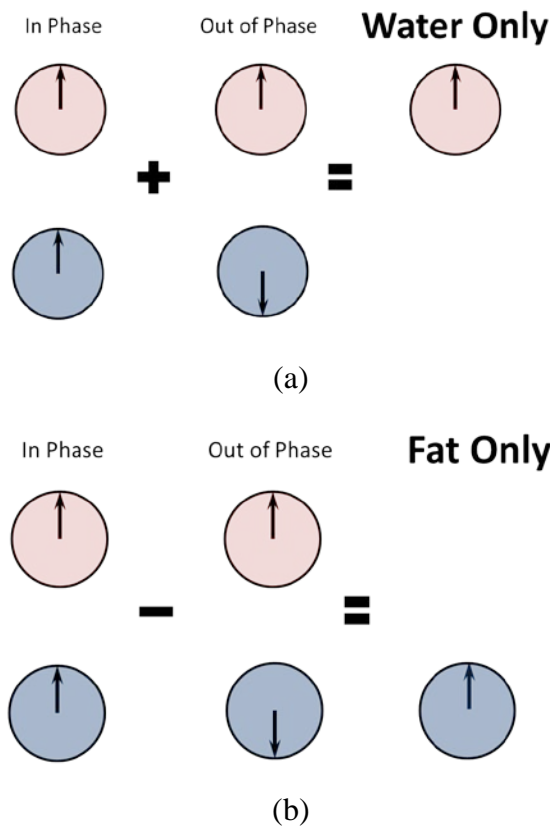


Figure 1-7: Two point Dixon method. Two images are acquired at different TE s when water and fat signal are in-phase and out-of-phase. By adding (a) and subtracting (b) these two images, water and fat images can be generated. This assumes a perfectly uniform B_0 magnetic field.

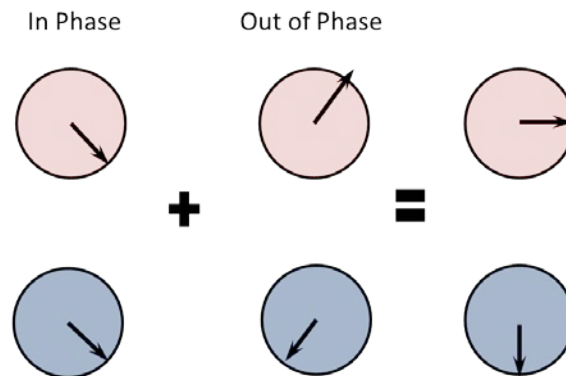


Figure 1-8: With non-uniform B_0 field, additional phase will accumulate. Simply adding and subtracting is not going to generate water and fat separated images.

to 0 and π . These two images are called in-phase (0) and opposed-phase (π) images. Since a homogeneous static field is assumed, the complex signals in a certain voxel are:

$$s_{in} = \rho_w + \rho_f , \quad \text{Eq. 1-43}$$

$$s_{op} = \rho_w - \rho_f . \quad \text{Eq. 1-44}$$

Then water and fat images can be solved easily:

$$\rho_w = \frac{1}{2}(s_{in} + s_{op}) , \quad \text{Eq. 1-45}$$

$$\rho_f = \frac{1}{2}(s_{in} - s_{op}) . \quad \text{Eq. 1-46}$$

Thus, by adding and subtracting in-phase and opposed-phase images, water only and fat only images are easily calculated. This is referred to as the two-point Dixon method, which is demonstrated in Figure 1-6.

1.3.2 Three Point Dixon Method

In the two-point Dixon method, a perfectly homogeneous main magnetic field is assumed; however, this is never the case in practice. Inhomogeneity of the main magnetic field can lead to water signal contaminating the “fat-only” image and fat signal contaminating the “water-only” image. At the point where there is main magnetic field offset, additional frequency from the magnetic field offset make water or fat protons not actually in-phase and out-of-phase when collected as seen in Figure 1-7. Adding and Subtracting in and out of phase images will not generate the correct answer. For this reason, a modified Dixon method was introduced that uses images acquired at three

different TEs to better estimate B_0 main field inhomogeneities (12). The signal can be modeled as below:

$$s(t) = (\rho_w + \rho_f \cdot e^{j2\pi ft}) \cdot e^{j\psi}, \quad \text{Eq. 1-47}$$

where f is the resonant frequency of fat relative to water described in Eq. 1-38, and ψ is the additional phase accumulation introduced in the water and fat signals by the B_0 field offset ΔB_0 . If a group of 3 different echoes are measured at specific TEs (Figure 1-8), which make the relative phases between water and fat $(-\pi, 0, \pi)$, then we can write the signals as:

$$s_{-1} = (\rho_w - \rho_f) \cdot e^{-j\psi}, \quad \text{Eq. 1-48}$$

$$s_0 = (\rho_w + \rho_f), \quad \text{Eq. 1-49}$$

$$s_1 = (\rho_w + \rho_f) \cdot e^{+j\psi}. \quad \text{Eq. 1-50}$$

From these equations, ρ_w , ρ_f and ψ can be determined. For those voxels where the phase offset ψ is greater than $\pm\pi$, ψ might be ambiguous and the fat and water signals can be swapped incorrectly.

The three-point Dixon method has shown unambiguous separation of water and fat components in the presence of B_0 field offsets greater than the chemical shift between water and fat two species (12). However, there might be places where the local field offset is so large that the unwrapping algorithm fails. The T_2^* decay effect between images collected at different TE is neglected; this causes problems in water and fat quantification (13,14). Also in this three point Dixon model, a relatively simple signal

model is used. It assumes that both water and fat have a single resonant frequency separated exactly by 3.5ppm. For most applications this is a satisfactory model and excellent qualitative water-fat separation can be achieved. However, it is well known that fat has a number of spectral peaks, as shown in Figure 1-9 (13,15). Thus more accurate fat water separation can be accomplished by correcting these confounding factors.

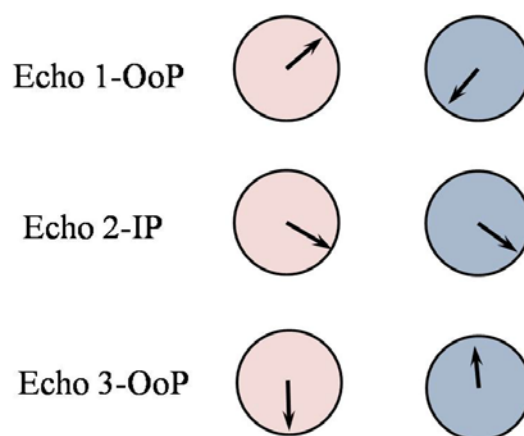


Figure 1-9: Three-point Dixon method. Images are collected at three different echoes, with the relative phases between water and fat are $(-\pi, 0, \pi)$.

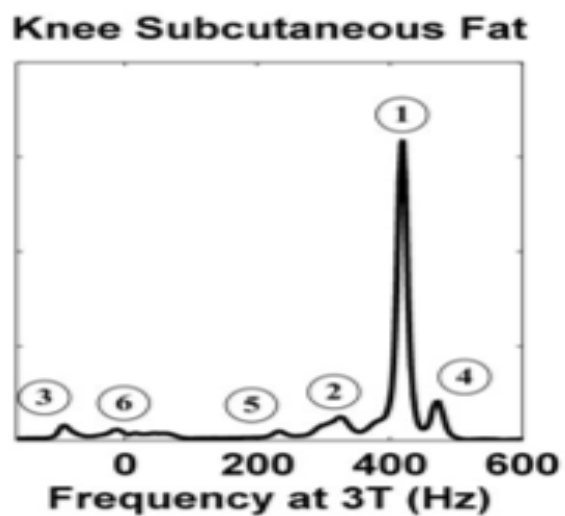


Figure 1-10: A representative spectrum collected in knee subcutaneous fat at 3T showing multi-peak pattern. Six peaks can be recognized and their relative chemical shift and amplitude can be calculated (13).

1.3.3 Multi-peak T_2^* Corrected IDEAL

The method used in this work to separate water from fat is called Iterative Decomposition of Water and Fat with Echo Asymmetric and Least-Squares Estimation (IDEAL) (16).

This method is developed to implement Dixon water-fat separation utilizing an iterative least-squares method that reconstructs data acquired at short echo time (TE) increments (16,17).

The signal is modeled as before:

$$s(t) = (\rho_w + \rho_f \cdot e^{j2\pi ft}) \cdot e^{j\psi}, \quad \text{Eq. 1-51}$$

where ρ_w and ρ_f are the signal intensity of the water and fat, f is the resonant frequency relative to water, ψ is the additional phase accumulation introduced by B_0 field inhomogeneity. If data are taken at discrete echo times, t_n ($n=1, \dots, N$), then

$$s_n = (\rho_w + \rho_f \cdot e^{j2\pi ft_n}) \cdot e^{j\psi} \quad \text{Eq. 1-52}$$

represents the signal in a specific pixel at echo time t_n . If an initial guess of ψ_0 is known, then the signal equation can be written as:

$$\hat{s}(t) = s_n \cdot e^{-j\psi_0} = \rho_w + \rho_f \cdot e^{j2\pi ft_n}. \quad \text{Eq. 1-53}$$

ρ_w and ρ_f can be solved in an iterative manner described as below:

1. Estimate the signal from each chemical species and an initial guess for the field map, ψ_0 . A useful initial guess for ψ_0 is zero (Hz).
2. Calculate the error to the field map, $\Delta\psi$.

3. Recalculate $\psi = \psi_0 + \Delta\psi$.
4. Recalculate \hat{s}_n with the new estimate of ψ .
5. Repeat the preceding three steps until $\Delta\psi$ is small.
6. Spatially filter (smooth) the final field map, ψ , with a low-pass filter.
7. Recalculate the final estimate of each chemical species image.

Note that in order to solve water and fat, it requires at least 3 images with different TE.

All the previous methods mentioned above are based on a relatively simple assumption that both water and fat have a single resonant frequency. Although for most applications this is a satisfactory model, it is not strictly true for fat. In general, fat has a number of spectral peaks as shown on Figure 1-9 (13,15,18). In particular, the peak from olefinic proton (5.3 ppm) is fairly close to the water peak. In the cases where accurate quantification of fat is desirable, the multiple peaks of fat must be considered (13).

The T_2^* decay of signal is also neglected in conventional two-point or three-point water fat separation techniques since T_2^* is much longer than TEs in most applications.

However, in some cases, especially liver with iron overload, T_2^* is much shortened. It is important to take T_2^* into account as well (14). Neglecting T_2^* decay will affect fat quantification even with long T_2^* (13,14). In the IDEAL iterative algorithm, T_2^* and fat signal interfere are addressed with the estimation of each other (8,13), as explained below.

A modified signal model that accounts for the multiple peaks of fat and T_2^* decay in the IDEAL reconstruction scheme was proposed by Yu et al (13).

In this proposed algorithm, signal from a single voxel containing water and fat can be modeled as:

$$s(t) = (\rho_w + \rho_f \sum_{p=1}^P \alpha_p \cdot e^{j2\pi f_p t}) \cdot e^{j\hat{\psi}}, \quad \text{Eq. 1-54}$$

where f_p is the resonant frequency of the p^{th} fat peak ($p = 1, \dots, P$) relative to water, and α_p the relative amplitude of the p^{th} peak, such that $\sum_{p=1}^P \alpha_p = 1$, $\hat{\psi}$ is the complex field map term, $\hat{\psi} = \psi + j / (T_2^* \cdot 2\pi)$, enabling estimation of T_2^* in addition to water and fat.

By collecting 6 points instead of 3 points, ρ_w , ρ_F (six different peaks are assumed) T_2^* and B_0^* can be all solved for using the iterative algorithm (13).

1.3.4 Multi-peak T_2^* IDEAL Fat Fraction

A quantitative description of the fat distribution is of great importance in the progression of Non-alcoholic Fatty Liver Disease as mentioned above. From the IDEAL technique, images containing only water and images containing only fat are generated. After water fat separation, a voxel by voxel fat signal fraction is computed as the quantitative endpoint, which will be given in the following content.

Let S_w and S_f denote the signal intensity in a pixel from the water and fat image respectively, fat signal fraction is defined as:

$$FF = \frac{S_f}{S_f + S_w} \times 100\% . \quad \text{Eq. 1-55}$$

Using this definition, the fat fraction provides a useful scale between 0% and 100%, which gives guidance in clinic application. Accurate fat fraction determination is only

possible with the consideration with multi-peak of fat spectrum as well as T_2^* correction (13).

However, fat fraction is a ratio on a voxel by voxel basis, which only provides a relative rather than an absolute measure in the tissue. This causes ambiguity when longitudinal monitoring of disease is necessary. In longitudinal study, when fat fraction changes, for example increases, fat fraction cannot distinguish whether the increase in fat fraction is caused by an increase in fat content, or a decrease in water content, or both. This issue is settled in chapter two where the absolute quantification is introduced.

1.4 Coil Sensitivity

Arrays of surface coils offer advantages in MRI: higher SNR and shorter data acquisition time through the use of parallel imaging (19-21). However, each surface coil has an inhomogeneous receiving sensitivity profile, referred to as its coil sensitivity, which results in pixel signal intensity variation across the field of view. The resulting surface coil signal intensities $S(\vec{r})$ at any pixel position \vec{r} can be described as the product of the true image $I(\vec{r})$ and its coil sensitivity profile at the same corresponding position $C(\vec{r})$

$$S(\vec{r}) = C(\vec{r}) \cdot I(\vec{r}) \quad \text{Eq. 1-56}$$

Given the coil sensitivities, Roemer *et al.* described a way to combine images from surface coils in such a way that SNR is optimized(21). In this algorithm, signal intensity for each voxel is calculated by combining coil data in the corresponding voxel using coil

sensitivity profiles. For a certain pixel, the expression for an SNR optimal combination of the coils with uniform signal intensity is as follows:

$$P = \lambda \frac{p^T R^{-1} c}{c^T R^{-1} c^*}, \quad \text{Eq. 1-57}$$

where P is the complex signal after coil combination, p is a complex column vector of signal intensity at each position, R^{-1} is the inverse of the noise correlation matrix, c is the column vector of coil sensitivity profile from each coil, and λ is a constant as a scaling factor (21). The noise correlation matrix can be calculated from noise recorded simultaneously from each coil in the array. Thus, getting accurate coil sensitivity profiles plays a key role in image reconstruction and must be carefully investigated.

Several approaches exist to measure coil sensitivity profiles, including direct calculation using the Biot-Savart law, estimation using root sum-of squares of individual coil images, and estimation using volume coil images. However, all of these methods have limitations outlined below.

Coil sensitivities can be calculated from the Biot-Savart law using the knowledge of geometry of the coil, object characteristics, and the resonant frequency (22). However, multiple limitations prevent practical use of this method. First, calculations are computationally intensive making efficient calculations for large coil arrays (8 or 32 channel) unfeasible. Second, the position of surface coils would depend on the patient anatomy thus requiring these calculations to be made for each scan individually (23).

Coil sensitivities can also be estimated using the root sum-of-squares (SoS) algorithm (21). Here, coil sensitivities are estimated by taking the ratio of the surface coil images to

the root sum-of-squares of the individual coil images. The SoS reconstructed image is modulated by a spatially varying function due to the non-uniformity of coil sensitivities (24). In absolute quantification applications, the ratio of signal in the pixel to be quantified and signal in a reference pixel is used for calibration of the measured signal intensity. Therefore, any spatially varying modulation of signal intensity is undesirable as it will introduce bias into the signal calibration.

Coil sensitivities can also be measured using an additional image acquisition of the patient using a volume coil. This volume coil can be used both to transmit the RF pulse used to produce the excitation flip angle and to receive the resulting signal. It is most often assumed that both the flip angle produced by the volume coil and its sensitivity to the received signal is uniform throughout its volume (i.e. it has a uniform transmit field and receive sensitivity). Here, coil sensitivities are estimated by taking the ratio of the surface coil images to the volume coil image (23,25), with the assumption that the receive sensitivity of the volume coil is constant throughout the field of view. In addition to equation Eq. 1-56, signal from acquisitions with the volume coil can be written as:

$$V(\vec{r}) = I(\vec{r}), \quad \text{Eq. 1-58}$$

provided there is a uniform volume coil sensitivity profile.

Combining Eq. 1-56 with Eq. 1-58, coil sensitivity profile can be solved as:

$$C(\vec{r}) = S(\vec{r}) / V(\vec{r}). \quad \text{Eq. 1-59}$$

This coil sensitivity profile then can be used in the coil combination process described in Eq. 1-57.

Even though one more acquisition with the volume coil is needed than for the SoS method, this method produces a much more accurate estimation of the true coil sensitivity than the other methods. However, the additional scan does bring some downsides. Patient motion between scans, as well as increased scan time, limits the potential application of this technique.

1.5 Flip Angle Mapping

1.5.1 Overview on Flip Angle Mapping

The knowledge of the B_1^+ field is crucial in quantitative imaging. The accuracy of these quantitative methods depends on accurate knowledge of the true flip angle. However, in high magnetic fields, 3T and above, the B_1^+ field of the volume coil cannot be assumed to be uniform any more. The wavelength of the B_1 field decreases linearly as the magnetic field strength increases. At 3T or above, the B_1^+ wavelength is getting close to the size of object being imaged, at which point it becomes impossible to avoid the destructive interference of the B_1^+ field (26).

Several methods exist for measuring the B_1^+ field, or the flip angle map. Many of these methods are based on the double angle method (DAM) (27). DAM based methods often require long repetition times and therefore long acquisition times. This makes them unsuitable for 3D abdominal experiments where short (<25s) acquisitions are required so that imaging can be completed within a single breath hold, thus avoiding motion artefacts caused by breathing. This acquisition time requirement drove us to choose the 3D Double Angle Look-Locker method proposed by Wade *et al* (28). Since it is the only flip angle

mapping method currently capable of mapping the 3D flip angle distribution in the abdomen rapidly enough to be acquired in a single breath hold.

1.5.2 Double Angle Method

If two images are acquired that differ only by their flip angle, and in particular if one flip angle is double the other, then the trigonometric double angle formula can be used to solve for the true flip angle. This is known as the double angle method (DAM) (27) and works as follows.

For a signal taken with unknown flip angle α , if the magnetization is fully relaxed, the signal is given by:

$$S_1 \propto M_0 \sin \alpha \quad \text{Eq. 1-60}$$

If the same experiment is repeated with twice the flip angle, $\alpha_2=2\alpha$, the signal in the second experiment is given by:

$$S_2 \propto M_0 \sin 2\alpha \quad \text{Eq. 1-61}$$

Using the double angle formula, α can be derived:

$$\alpha = \arccos\left(\frac{S_2}{2S_1}\right) \quad \text{Eq. 1-62}$$

Assuming relative image phase is maintained, the technique is valid for flip angles ranging from 0 to π . However the apparent downside of this application is the lack of acquisition time efficiency. The requirement that the magnetization should be fully recovered before each RF pulse requires that the interval between acquisitions of each RF pulse (the repetition time (TR)) must be at least five times T_1 . Abdominal T_1 values are

on the order of 1s so the TR must be approximately 5s. Since acquisition of an image requires many signal excitations (typically one excitation per phase encode), the lengthy TR makes the DAM time consuming and not applicable to 3D abdominal flip angle measurements.

1.5.3 Look-Locker Sequence

The Look-Locker method was first developed as a time efficient method to measure the longitudinal recovery constant T_1 (29). This experiment is shown in Figure 1-10 (28).

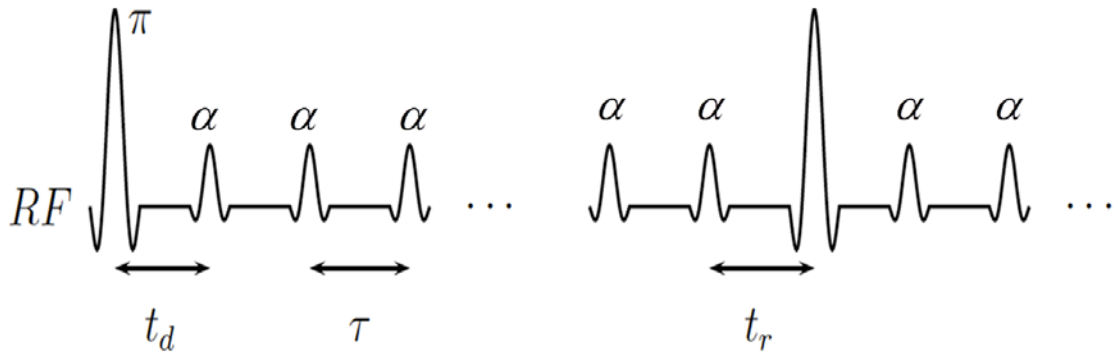


Figure 1-11: Conventional Look-Locker sequence. An image is created for each α sampling pulse, and t_d and t_r are the time delays before and after the α -pulse train, τ is the repetition time.

The small α pulses that follow the inversion pulse (π) cause the recovery of the longitudinal magnetization to occur with an apparent rate T_1^* instead of T_1 . Under the small flip angle assumption, this new longitudinal relaxation constant can be defined:

$$\frac{1}{T_1^*} = \frac{1}{T_1} - \frac{\ln(\cos \alpha)}{\tau}, \quad \text{Eq. 1-63}$$

where α is the flip angle of the RF pulse, τ is the repetition time of the α pulse, and T_1 is the true longitudinal recovery constant. Since T_1 is related to T_{1}^* through known variables (α and τ), it is possible to calculate T_1 easily after fitting the recovery curve for T_{1}^* . Because multiple points can be sampled along the recovery curve, the data for calculating T_1 can be acquired far more efficiently than with standard inversion recovery methods(28). These methods have been extended to 3D volume acquisition (30).

1.5.4 Flip Angle Measurement with the Double Angle Look-Locker Sequence

Using the Look- Locker sequence, two measurements with low flip angles α and 2α are taken. Recovery constants can be described as below:

$$\frac{1}{T_{1,1}^*} = \frac{1}{T_1} - \frac{\ln(\cos \alpha)}{\tau}, \quad \text{Eq. 1-64}$$

$$\frac{1}{T_{1,2}^*} = \frac{1}{T_1} - \frac{\ln(\cos 2\alpha)}{\tau}. \quad \text{Eq. 1-65}$$

This equation set can be solved for the true flip angle $\alpha_{DALLtrue}$ in the double angle Look-Locker (DALL) sequence. The following content gives a detailed solution.

T_1 can be removed by combining Eq. 1-64 and Eq. 1-65, leaving:

$$\frac{1}{T_{1,1}^*} + \frac{\ln(\cos \alpha)}{\tau} = \frac{1}{T_{1,2}^*} + \frac{\ln(\cos 2\alpha)}{\tau}. \quad \text{Eq. 1-66}$$

Rearrange this equation we can get:

$$\frac{\tau}{T_{1,1}^*} - \frac{\tau}{T_{1,2}^*} = \ln\left(\frac{\cos 2\alpha}{\cos \alpha}\right). \quad \text{Eq. 1-67}$$

This gives us:

$$\exp\left(\frac{\tau}{T_{1,1}^*} - \frac{\tau}{T_{1,2}^*}\right) = \frac{\cos 2\alpha}{\cos \alpha}. \quad \text{Eq. 1-68}$$

Let $E_{\Delta} = \exp\left(\frac{\tau}{T_{1,1\alpha}^*} - \frac{\tau}{T_{1,2\alpha}^*}\right)$ and using the double angle formula $\cos(2\alpha) = 2\cos^2(\alpha) - 1$

we get:

$$2\cos^2(\alpha) - E_{\Delta}\cos(\alpha) - 1 = 0. \quad \text{Eq. 1-69}$$

and the actual flip angle is:

$$\alpha = \arccos\left[\frac{1}{4}(E_{\Delta} + \sqrt{E_{\Delta}^2 + 8})\right], \quad \text{Eq. 1-70}$$

where

$$E_{\Delta} = \exp\left(\frac{\tau}{T_{1,1\alpha}^*} - \frac{\tau}{T_{1,2\alpha}^*}\right). \quad \text{Eq. 1-71}$$

In this thesis, I am going to implement a combination of those methods mentioned above, to generate a mass density map in the abdomen. I am going to use Multi-peak T_2^* IDEAL sequence to separate water fat signal. A phantom with known mass density will be used to calibrate the conversion for signal intensity to mass density. In order to do an accurate conversion, coil sensitivity and flip angle are going to be corrected using those method described above. The objective of this thesis is to demonstrate the feasibility of using these methods to quantify fat and water mass density in the liver.

Chapter 2

2 Absolute Water and Fat Quantification Using MRI

2.1 Introduction

Absolute quantification of fat in mass density is of great value for a variety of applications. Such applications could include but not be limited to the evaluation of progression and monitoring the effectiveness of treatment of diseases like obesity, or non-alcoholic fatty liver disease (NAFLD).

Obesity is increasingly affecting Western world. It causes the accumulation of adipose tissue and can lead to increased fat content in organs like skeletal muscles and liver. In children, it is the major risk for developing Metabolic Syndrome (MetS) (4). NAFLD is the hepatic manifestation of syndrome MetS (31) and is characterized by the accumulation of fat in the liver cells. Invasive needle biopsy of the liver is the current gold standard for diagnosis of NAFLD. However, in addition to its inherent risks, it suffers from considerable potential sampling error (8,32). Therefore, there is considerable interest in developing non-invasive methods to measure the distribution of fat content in the liver.

Quantitative water-fat MRI has been investigated as a non-invasive alternative to biopsy. The current biomarker typically reported for quantitative MRI is the relative fat signal fraction. Accurate 3D measurement of fat signal fraction (fat signal intensity as a fraction of the sum of fat and water signal intensity) on pixel-by-pixel basis has been demonstrated with IDEAL (**I**terative **D**ecomposition with **E**cho **A**symmetric and **L**east square estimation) (9,16). However, in longitudinal studies, knowing only the change in fat fraction is not enough to tell whether the change is caused by changes in the absolute

amount of fat or of water, or both. In this work we demonstrate a fast absolute quantitative approach to overcome this weakness.

Several absolute quantitative MRI methods have been proposed by Shah et al. for water content (33,34) and Hu et al. for water and fat content (35) . The basic idea of their experiments is to combine *in vivo* proton density weighted imaging with a reference signal from phantom with known mass density. By calibrating signal intensity with known mass density of the phantom, absolute fat and water in unit of mass (e.g. grams) can be calculated. However, each of their methods has some limitations.

Shah et al. managed to quantitatively map cerebral water content with full brain coverage in 10 min. (34). Multi-echo gradient echo **Quantitative T_2^* Image(QUTE)** sequences and echo planar imaging (EPI) were used to acquire images (33). After collecting data with different repetition times and/or flip angles, T_1 , T_2^* and the transmit B_1^+ field (excitation flip angle) were calculated and corrected. This method was capable of using coil arrays for signal reception, once appropriate corrections for receive coil sensitivity were made (34). However, because this method had been applied primarily in the brain where there was very little fat content, no attempt was made to distinguish between water and fat signal. The implicit assumption that all signal comes from water would lead to error when fat was present, as would be the case when evaluating NAFLD. Moreover, this method would be challenging to apply in the abdomen due to the lengthy acquisition time.

Hu et al. used the IDEAL sequence to separate water and fat on a voxel by voxel basis. Low flip angles were used to minimize T_1 effects so that proton density weighted images

were produced (35). However T_2^* relaxation is not considered in their work, even though it has been shown to be essential for accurate water-fat separation (13). To minimize the RF non-uniformity, a single-channel transmit and receive birdcage coil was used, severely limiting the SNR of the method. Also, B_1^+ excitation flip angle distributions were measured by the saturated double-angle method (SDAM) (35) which is neither time efficient nor accurate enough for B_1^+ measurement in the abdomen. This inability to perform flip angle calibration quickly enough for breath hold imaging limited this method to only phantom experiments and *ex vivo* swine experiments.

To avoid the limitations mentioned above in absolute quantification of water and fat content, we propose an extension of the works of Shah et al. and Hu et al. In this proposed method, the IDEAL sequence is used to acquire fat and water separated images. By using receiver coil arrays and parallel imaging reconstruction, the data acquisition time is shortened to be compatible with imaging during a ~20 s breath hold, allowing applications in the human abdomen. The individual coil sensitivity profiles are calculated and signal-to-noise ratio (SNR) optimal receive sensitivity corrected images are reconstructed. Rapid 3D B_1^+ transmit field measurement is accomplished in a breath hold acquisition, allowing flip angle correction to be performed in the abdomen. After all those corrections, absolute fat and water mass density is computed with the phantom as a reference. The feasibility of simultaneous quantification of water and fat is demonstrated in phantoms and in the human abdomen.

2.2 Theory

T_1 independent, T_2^* corrected chemical shift based water-fat separation methods with accurate spectral modeling of fat can be used to produce water-only and fat-only images where signal intensity is proportional to proton density (36); however, the proportionality constant is usually unknown so signal intensity can't be converted directly to absolute mass density.

Placing a reference phantom (e.g. pure water), whose mass density is known a priori, in the field of view during the measurement allows calibration of the signal intensity so it can be converted to absolute mass concentration. The absolute mass of water m_w and fat m_f can be calculated on a voxel by voxel basis as below:

$$D_{w,f}(\vec{r}) = \left(\frac{\rho_{w,f}(\vec{r})}{\rho_{ref}} \right) \cdot D_{ref}, \quad \text{Eq. 2-1}$$

where $\rho_{w,f}(\vec{r})$ denotes the water or fat proton density weighted signal at voxel \vec{r} , ρ_{ref} is the proton density weighted signal of pure water or fat phantom, D_{ref} is the mass density of the reference phantom and $D_{w,f}$ is the water or fat mass density (33-35).

Absolute quantification is not accurate unless all the sources of bias are considered and properly corrected. These corrections include: B_1^+ transmit field inhomogeneity of the Volume transmit Coil ($k_{B_1^+}^{vc}$), B_1^- receive inhomogeneity of the Phased array ($k_{B_1^-}^p$) used for signal acquisition and T_1 and T_2^* relaxation in the tissues being measured. In IDEAL acquisitions, low flip angles are used to minimize the T_1 effect (36) and T_2^* is corrected

in the IDEAL reconstruction (13), so we only need to deal with transmit and receive inhomogeneity here. Let $S_{w,f}(\vec{r})$ and $S_{ref,w,f}$ denote the original signal from IDEAL (T_1 effect minimized, T_2^* corrected) at voxel \vec{r} and the pure water reference phantoms. Then we have:

$$\frac{\rho_{w,f}(\vec{r})}{\rho_{ref}} = \frac{S_{w,f}(\vec{r}) \cdot k_{B_1^+}^{vc}(\vec{r}) \cdot k_{B_1^-}^p(\vec{r})}{\langle S_{ref,w,f} \cdot k_{ref,B_1^+}^{vc} \cdot k_{ref,B_1^-}^p \rangle}, \quad \text{Eq. 2-2}$$

where $\langle S_{ref} \rangle$ is the average signal intensity over all voxels contained in the reference phantom (34), $k_{B_1^+}^{vc}$ is the correction factor for B_1^+ transmit field inhomogeneity and $k_{B_1^-}^p$ is the correction factor for B_1^- receive field inhomogeneity. By inserting Eq. 2-2 to Eq. 2-1, the absolute mass of water and fat can be shown to be:

$$D_{w,f}(\vec{r}) = \frac{S_{w,f}(\vec{r}) \cdot k_{B_1^+}^{vc}(\vec{r}) \cdot k_{B_1^-}^p(\vec{r})}{\langle S_{ref,w,f} \cdot k_{ref,B_1^+}^{vc} \cdot k_{ref,B_1^-}^p \rangle} \cdot D_{ref}, \quad \text{Eq. 2-3}$$

where D_{ref} is the mass density of the reference phantom and $D_{w,f}$ is the water or fat mass density.

2.2.1 B_1^+ Transmit Field Inhomogeneity Factor $k_{B_1^+}^{vc}$

The flip angle we request in the IDEAL experiment ($\alpha_{IDEALnom}$) will not be the true flip angle actually seen by the sample ($\alpha_{IDEALtrue}$) due to the B_1^+ transmit field inhomogeneity of the volume coil. Therefore, we need to map the B_1^+ excitation profile of the volume coil and get the correction factor $k_{B_1^+}^{vc}$. The flip angle distribution is measured using the

double angle Look-Locker technique (DALL) (28). The flip angle measured using DALL ($\alpha_{DALLtrue}$) is compared to the nominal flip angle prescribed in the DALL experiment ($\alpha_{DALLnom}$) to correct the nominal flip angle prescribed in the IDEAL acquisition ($\alpha_{IDEALnom}$):

$$\alpha_{IDEALtrue} = \alpha_{IDEALnom} \cdot \frac{\alpha_{DALLtrue}}{\alpha_{DALLnom}}. \quad \text{Eq. 2-4}$$

Based on Eq. 2-4, $k_{B_1^+}^{vc}$ can be determined as:

$$k_{B_1^+}^{vc} = \frac{1}{\sin(\alpha_{IDEALtrue})}. \quad \text{Eq. 2-5}$$

2.2.2 B_1^- Phased Array Receive Field Sensitivity Profile c

The sensitivity profile of the receive phased array can be calculated if another volume coil receiving experiment is added. In the phased array experiment, the flip angle is produced with the volume coil and signal is received with surface coils. Therefore, in order to recover proton density ρ , signal S_p should be corrected by transmit $k_{B_1^+}^{vc}$ correction factor and receive correction factor $k_{B_1^-}^p$:

$$\rho = S_p \cdot k_{B_1^-}^p \cdot k_{B_1^+}^{vc}, \quad \text{Eq. 2-6}$$

where ρ is the proton density in a certain voxel.

In the volume coil experiment, the same coil is used to produce the flip angle and receive the resulting signal. Therefore the proton density we get from the same voxel will be :

$$\rho = S_{vc} \cdot k_{B_1^-}^{vc} \cdot k_{B_1^+}^{vc}. \quad \text{Eq. 2-7}$$

Combining equations Eq. 2-6 and Eq. 2-7, we can get:

$$k_{B_1^-}^p = \frac{S_{vc} \cdot k_{B_1^-}^{vc}}{S_p}. \quad \text{Eq. 2-8}$$

This is problematic as we have not measured the receive field of the volume coil. At low values for B_0 (≤ 1.5 T) it is reasonable to assume that $k_{B_1^-}^{vc}$ is a constant, and can therefore be safely ignored. This is precisely the assumption made in coil array sensitivity measurement in parallel imaging methods like SENSE (37). However, at higher field strengths, such as the 3.0 T field we used for our measurements, it is no longer safe to assume that $k_{B_1^-}^{vc}$ is a constant.

However, we have measured $k_{B_1^+}^{vc}$ in the previous flip angle calibration step. If we assume that the volume coil receiving profile is approximately equal to its transmitting profile, (i.e. $k_{B_1^-}^{vc} = k_{B_1^+}^{vc}$) then we finally get:

$$k_{B_1^-}^p = \frac{S_{vc} \cdot k_{B_1^+}^{vc}}{S_p}. \quad \text{Eq. 2-9}$$

Our coil sensitivity map is just the reciprocal of $k_{B_1^-}^p$:

$$c = \frac{1}{k_{B_1^-}^p} = \frac{S_p}{S_{vc} \cdot k_{B_1^+}^{vc}}. \quad \text{Eq. 2-10}$$

The assumption that $k_{B_1^-}^{vc} = k_{B_1^+}^{vc}$ is reasonable at intermediate B_0 field strengths, but will break down at higher fields like 7.0 T where $k_{B_1^-}^P$ and $k_{B_1^+}^P$ become significantly different (32).

2.2.3 Image Reconstruction

To acquire all the data necessary to produce fat-water separated images corrected for B_1^+ and B_1^- inhomogeneity we follow the following procedure:

- 1) Acquire data suitable for IDEAL fat-water separation using a phased array coil (S_p).
- 2) Repeat step 1, except acquire data with a volume coil (S_{vc}).
- 3) Obtain a pixel by pixel B_1^+ transmit correction factor $k_{B_1^+}^{vc}$ by flip angle maps over the volume imaged in Step 1 using double angle Look-Locker technique (28).
- 4) Generate B_1^- (coil sensitivity) maps were generated using the method described as Eq. 2-10 (37).
- 5) Combine the IDEAL data from the phased array using Roemer's uniform sensitivity SNR optimal method that corrects for the non-uniform coil sensitivity c (21).
- 6) Reconstruct the B_1^- corrected, coil combined IDEAL data with T_2^* IDEAL to produce fat-water separated images that were corrected for T_2^* variations.
- 7) Correct the T_2^* corrected IDEAL images for flip angle variations using the B_1^+ map from step 4 (apply correction factor $k_{B_1^+}^{vc}$) (34).

- 8) Finally, use the signal intensity of pure water phantom (which has a known proton density) calibrate the signal intensities of the water-only and fat-only images produced in step 7 and convert the signal intensity to units of density or mass (34).

This procedure is summarized graphically in Figure 2-1.

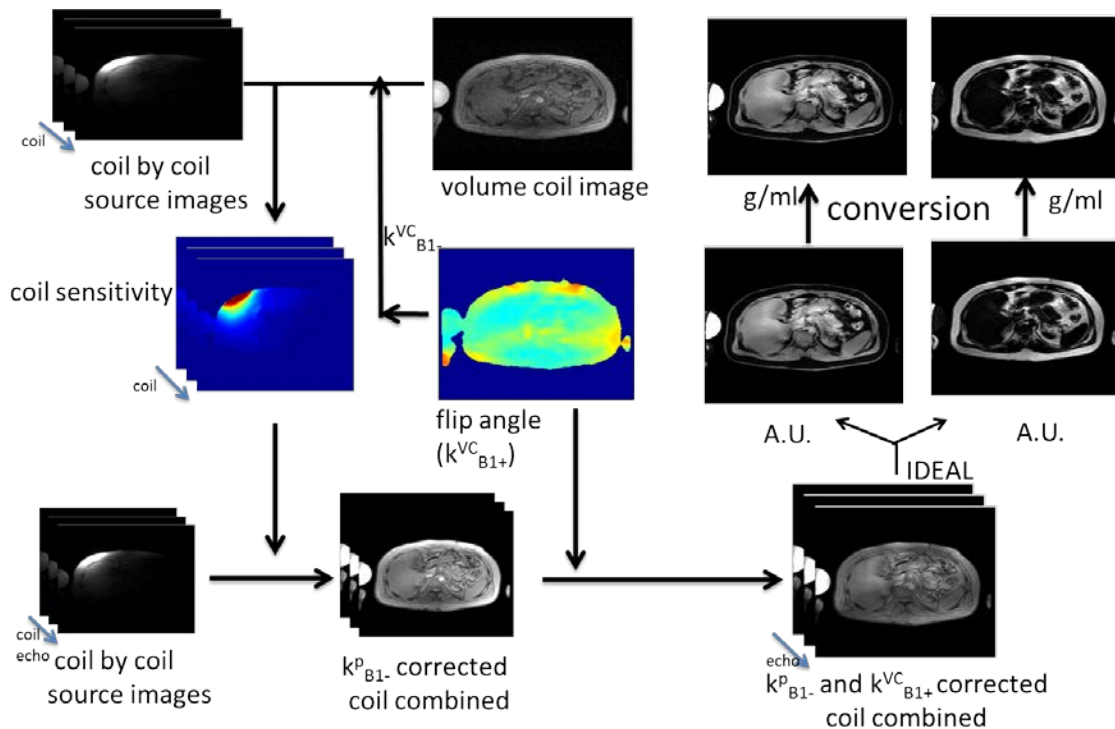


Figure 2-1: Flow chart of image acquisition and reconstruction. Flip angle maps were acquired for both k_{B1+}^{vc} and c correction. The volume coil image was first corrected for $B1^-$ using flip angle map as an approximation. Images from phased array were divided by the volume coil image to generate the phased array surface coil sensitivity maps. With these maps, coil by coil images were combined. Then those corrected images were run through the IDEAL reconstruction to get water

and fat separated images with arbitrary units. By calibrating with a phantom with known proton density, water and fat mass maps were generated.

2.3 Methods

All the experiments were conducted on 3.0 T MRI system (Discovery MR 750, GE Healthcare, Waukesha, WI) using 6 echo Multi-peak T_2^* corrected IDEAL sequence. The phantoms were at room temperature.

2.3.1 Phantom Experiments

Eight vials of homogeneous emulsions of different concentrations of peanut oil and water (0%, 5.0%, 10.0%, 15.0%, 20.0%, 30.0%, 40.0%, and 100% volume fraction of fat) were used in this experiment. The emulsions were prepared with sodium dodecyl sulfate and agar to stabilize the emulsions (38). Images were acquired with an eight-channel head array and a volume coil. IDEAL imaging parameters were: Flip angle = 3 degree, TR=6.3215ms, six echoes at TE= = [0.768 1.364 1.960 2.556 3.152 3.548] ms, Echo Train Length (ETL)=2, $N_x=128$, $N_y=128$, FOV=24cm x 24cm, 16 slices at thickness=5 mm. A 3D double angle Look-Locker sequence was used to generate a B_1^+ (flip angle) map, which was acquired with the following parameters: TR=minimum, $N_x=32$, $N_y=32$, FOV=26cm×26cm, 16 slices at thickness=5 mm. The IDEAL images were corrected for B_1^+ and B_1^- inhomogeneity as described above, then calibrated with the 0% (pure water) and 100% (pure peanut oil) fat fraction phantoms.

2.3.2 In Vivo Experiments

Following REB approval and obtaining informed consent, *in vivo* IDEAL data were collected from the calf and abdomen of a healthy volunteer.

In the calf experiment, an 8-coil abdominal array and volume coil were used. IDEAL imaging parameters were: Flip angle = 3 degree, TR=6.3215ms, six echoes at TE= [0.768 1.364 1.960 2.556 3.152 3.548] ms, Echo Train Length (ETL)=3, $N_x=192$, $N_y=192$, FOV=38cm×28.5cm, 16 slices at thickness=5 mm. A 3D double angle Look-Locker sequence was used to generate B_1^+ (flip angle) map, which was acquired with the following parameters: TR=minimum, $N_x=32$, $N_y=32$, FOV=38cm x 28.5cm, 16 slices at thickness=5 mm.

In the abdomen experiment, 32-channel abdominal array and volume coil were used. IDEAL imaging parameters were: Flip angle = 3 degree, TR=5.8080ms, six echoes at TE= [0.768 1.364 1.960 2.556 3.152 3.548] ms, Echo Train Length (ETL)=3, $N_x=128$, $N_y=128$, FOV=46cm×34.5cm, 16 slices at thickness=3mm. A 3D double angle Look-Locker sequence was used to generate B_1^+ (flip angle) map, which was acquired with the following parameters: TR=minimum, $N_x=32$, $N_y=32$, FOV=46cm x 46cm, 16 slices at thickness=3 mm.

2.4 Result

2.4.1 Phantom Experiments

Figure 2-2 shows the water and fat mass density maps for a slice through the water-fat phantoms set. The top two images are water and fat mass density maps without flip angle (B_1^+) correction. A sum of squares coil combination that was automatically applied in the parallel MRI reconstruction process partially addressed the receiving field (B_1^-) inhomogeneity in the uncorrected images. It can be seen that the bottom part of the uncorrected water image appears brighter than the top part. This is expected, as the

bottom part is closer to the receive coils, leading to higher signal intensity. The bottom two images are the water and fat images after flip angle (B_1^+) and coil sensitivity (B_1^-) correction. Signal intensity is more uniform across the whole volume after correction.

Regions of interest (ROI) were taken from the uncorrected images and corrected mass density maps on each individual vial. Figure 2-3 plots the calibrated water and fat mass density in each vial against the known water and fat mass density. Differences between the measured mass densities to the actual mass density were dramatically reduced when both flip angle and coil sensitivity were properly corrected. A linear fit to the fat mass density data demonstrates excellent agreement and validates the accuracy of correction factors applied to data. The line of best fit has a slope of 0.99, and intercept of 0.02 mg/ml and a correlation coefficient of $R_2 = 0.99$.

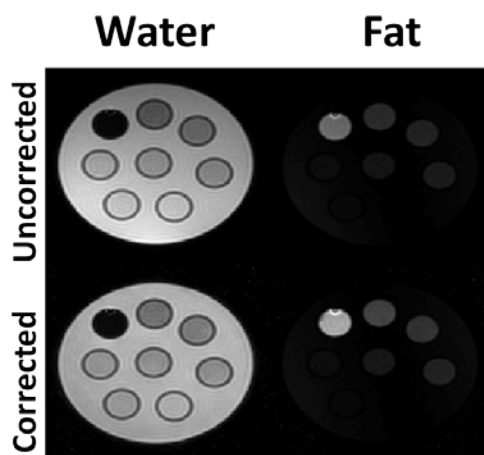


Figure 2-2: Phantom result. Top two images are water and fat mass density map before all the correction, bottom two images are water and fat mass density map.

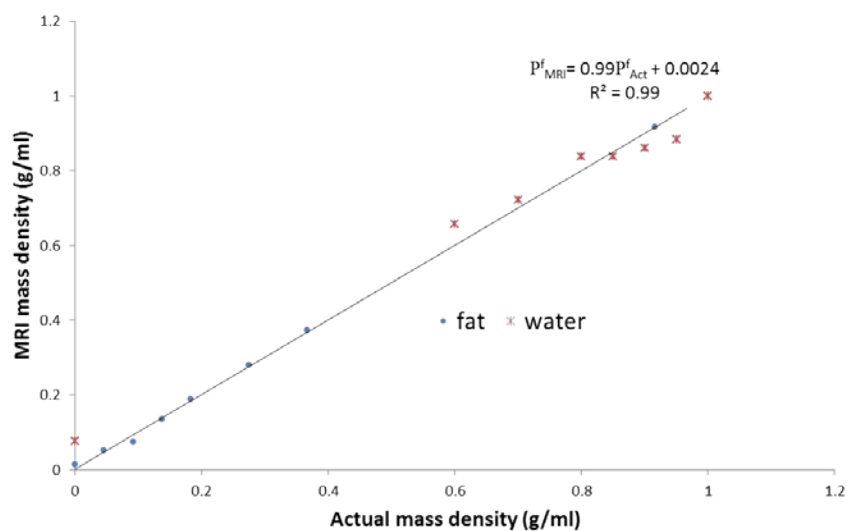


Figure 2-3: Calibrated water and fat mass density in each vial against the known water and fat mass density. Linear regression shows slope of 0.99, and intercept of 0.002 g/ml and a correlation coefficient of $R^2 = 0.99$.

2.4.2 In Vivo Experiments

Figure 2-4 shows a water and mass density map of a volunteer's calves. A bottle of pure peanut oil was placed between calves in the field of view as proton density reference. The corrected water and fat images are noticeably more uniform than the uncorrected images, particularly at the periphery. A ROI was taken in the muscle and the mass density of water content was determined to be 0.80 g/ml, with a standard deviation of 0.08 g/ml. This result is an excellent match with the literature value of 0.78 g/ml (39).

Figure 2-5 gives the result of reconstructed mass density map of an axial slice in the abdomen of the human. Again, ROIs were placed in different tissues. MRI measured water mass density of the right lobe of the liver is 0.79 g/ml, with a standard deviation 0.09g/ml, which is a good match for the expected value of 0.72 g/ml (40).

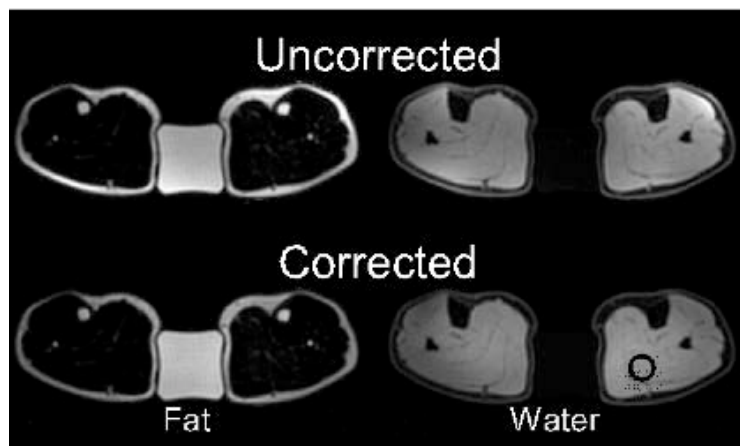


Figure 2-4: *In vivo* images of a volunteer's calves. (The object between the calves is a pure fat mass density reference.) The corrected water and fat images are noticeably more uniform than the uncorrected images, particularly at the periphery. The circle in the corrected water image indicates the ROI in which muscle density was measured.

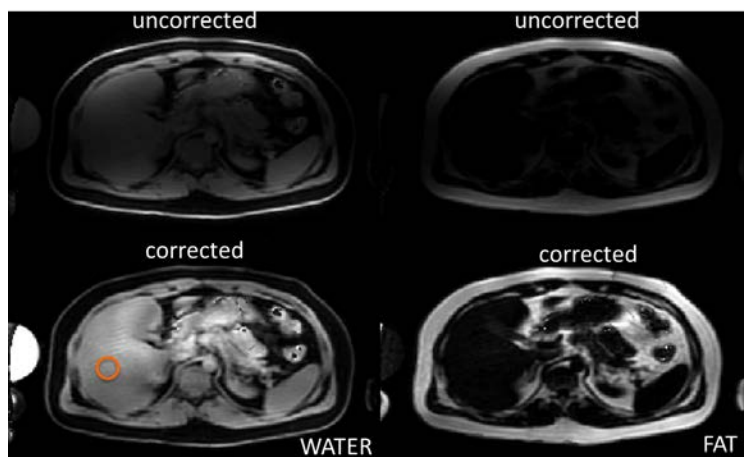


Figure 2-5: *In vivo* images of a volunteer's liver. (The object beside the abdomen is a bottle of water as mass density reference.) The corrected water and fat images are noticeably more uniform than the uncorrected images across the liver. The circle on the corrected water image indicated the liver density measurement location.

2.5 Discussion

We have demonstrated the feasibility of absolute quantification of water and fat in abdomen. Phantom experiments showed that after correction and calibration, the result from MRI measured absolute fat and water content agreed very well with the true fat and water concentration. In the *in vivo* experiment, MRI measurement of the fat and water densities of calf, liver and other tissues also agreed with literature values.

The use of a rapid B_1^+ transmit field mapping sequence made it possible to map the flip angle profile within one breath hold, which was crucial to allowing these measurements to be made in the abdomen. The use of a phased array for data acquisition enabled the use of parallel imaging to accelerate IDEAL data acquisition sufficiently to allow imaging in the abdomen. Multi-peak T_2^* IDEAL sequence gave us perfectly separated water fat images without T_2^* bias (13,38). It provides a more accurate water fat separation from the old version IDEAL which is using in previous work (35). Previous approaches to absolute water and fat quantification have used some subset of these corrections, but this is the first time all of these corrections have been used in combination to allow absolute quantification in the human abdomen.

In traditional determination of phased array coil sensitivity c , images from each single coil are directly divided by the volume coil image. The procedure assumes the volume coil has uniform B_1 transmit and receive field (23,25,37). This is a good approximation at low main magnetic field strengths. However, when the field strength increases above 3T, identical excitation and reception profiles are not an acceptable assumption anymore, especially in quantitative imaging techniques. In this work, instead of assuming a uniform

volume coil profile, we made the assumption that the receiving profile of volume coil is the same as its transmitting profile (flip angle map), which can be measured by DALL (28). By correcting for the receiving profile by flip angle map, result is improved as we see in Figure 2. At very high field strengths (7T or above) where the assumption that B_1^- equals B_1^+ is no longer true(32), this reconstruction scheme might fail. At these higher field strengths it would be necessary to separately measure the B_1^- and B_1^+ fields.

After inhomogeneous intensity of surface coil being carefully corrected, phased array can be used for data acquisition. This benefits us with not only higher SNR but also the capability of parallel imaging. The data acquisition time is significantly shortened with parallel imaging, which enables the technique applicable to *in vivo* abdominal applications.

We did not attempt to correct our calibration for the effects of temperature on the density of the reference phantom. Since the reference phantom was at room temperature, which is different from the temperature in tissue, some bias may have been introduced by the higher density of water in the room temperature phantom. This source of bias could be corrected by pre-heating the reference phantom to body temperature, or by explicitly compensating for the effect of temperature on water density. However, given the excellent match between our *in vivo* density measurements and the expected values, we feel that the effect of temperature on our density calibration was minimal.

Water and fat have different T_1 values both in phantoms and *in vivo*, and this could bias our results. In this work, all experiments were using low flip angle (1 or 3 degrees) to minimize T_1 bias, by ensuring all our images were proton density weighted. The effect of

T_1 bias correlates with the flip angle used for data acquisition, with bigger flip angles introducing more T_1 bias (36). The price paid for reducing T_1 bias using small flip angle acquisitions is a reduction in image SNR, thus resulting in poor precision in the quantitative measurements. Methods to eliminate T_1 bias while still using higher flip angles to improve SNR are being investigated(41). Should these methods prove successful, they could be integrated with the method we have described here to further improve the precision of these measurements.

2.6 Conclusion

In conclusion, the accurate estimation of water and fat content *in vivo* has been demonstrated and validated. Using this method, absolute water and fat content can be computed and visualized as a mass density map. Future application of this method to cardiac imaging remains to be investigated.

Chapter 3

3 Summary and Future Work

3.1 Summary

Quantitative MRI is playing a more and more important role in diagnosing and staging diseases in the clinic. Quantitative water and fat imaging is especially attractive as many diseases, such as Non-Alcoholic Fatty Liver Disease (NAFLD), brain edema, brain tumors and metastases, are associated with changing in either water or fat content in tissue. Quantitative MRI offers a non-invasive method to track those changes in disease progression. The current endpoint reported is to use fat-water signal fraction as a biomarker for fatty liver disease. In this work, the end point for quantitative water and fat imaging has been refined one step further, so that absolute water or fat mass can be reported.

By carefully considering and correcting all the relevant confounding factors, a fast accurate absolute quantification of water and fat content was demonstrated to be feasible *in vivo*. In the following subsections, I will summarize all the fundamental modifications that have been made and how they relate to obtain an accurate absolute map of water and fat content over the liver or leg.

In order to validate the image reconstruction algorithm, a phantom study with 8 channel head coil was performed. Phantoms with known water and fat concentration were imaged with IDEAL sequence. A pure phantom with known proton density was put in the field of view as a calibration reference. Volume coil image was taken at the same TE as reference to calculate surface coil sensitivity. Separate acquisition with Double Angle Look-Locker was collected for the flip angle map. After coil combination and flip angle correction, images were run through IDEAL reconstruction algorithm to get water and fat separated

images. Final step was to convert those water fat images with arbitrary units in to images with unit of mass density. The regression line of experimental result to actual mass density has a slope of 0.99, which validated the feasibility of this method.

In vivo experiments were done on a healthy volunteer. Following the same procedure with the phantom study described as above, absolute water and fat distributions were acquired. Water densities measured from regions of interest in the calf muscle and the liver agreed with previously reported literature values.

Comparing to existing methods for absolute water and fat quantification, several improvements have been made in this work which have made absolute fat and water quantification in the abdomen possible for the first time. These include modified coil sensitivity correction and fast 3D flip angle mapping (DALL). I modified the standard coil sensitivity calibration methods to account for volume coil receive inhomogeneity. This resulted in more accurate measurement of phased array coil sensitivity, thereby allowing IDEAL acquisition with phased arrays. This increased the SNR of my measurements and made it possible to use parallel imaging to accelerate data acquisition. This accelerated data acquisition was critical for making it possible to acquire the data needed for quantitative measurement of water and fat in the abdomen where it is necessary to acquire the images within a short breath hold.

With the DALL method, it was possible to measure the flip angle distribution over the entire 3D volume that was also imaged in the IDEAL acquisition. The accurate flip angle map enabled correction of B_1^+ non-uniformity in the reconstructed IDEAL images. By assuming $k_{B_1^-}^{vc} = k_{B_1^+}^{vc}$, the accuracy of the phased array coil sensitivity estimation was also

improved. Because DALL data acquisition time was as short as 20 seconds, it was possible to map the flip angle distribution within a breath hold, thus allowing application of flip angle mapping to abdominal imaging.

3.2 Future work

3.2.1 T_1 Correction

Signals acquired from the SPGR sequence depend on the proton density ρ , relaxation time T_1 and T_2^* , repetition time TR, echo time TE and the true flip angle α . Since TR and TE can be measured accurately, the confounding factors come down to T_1 , T_2^* and α . In this work, corrections on T_2^* and flip angle α have already been carefully considered. In terms of the relaxation parameter T_1 , since extremely small flip angles were used (3°), the confounding effect from T_1 bias was assumed to be negligible. However, it is known that water and fat have different T_1 values (36). According to simulations in a previous study (36), at a 10 degree flip angle, the signal from fat can be as much as 30% higher than that from water. Using low flip angle can minimize this effect, but the trade-off is relatively low SNR.

T_1 correction could be added to improve the algorithm presented in this thesis. One possible option is to use estimated T_1 values to correct for the T_1 difference between water and fat (41). By using literature values, T_1 bias can be significantly reduced. Thus, a high flip angle can be used to increase SNR. Another alternative is to add another measurement to get the actual T_1 values. Multiple methods are reported previously, such as traditional inversion recovery pulse (42), 3D MAPSS (43) or other T_1 mapping methods (44,45). However, these methods are time consuming due to the need to invert

the longitudinal magnetization and then allow it to recover. Even accelerated T_1 measurement methods, such as DESPOT and Look-Locker are not fast enough to be feasible in abdominal imaging (46-48). With future work on time efficient T_1 correction, larger flip angles could be used in this experiment to increase SNR.

3.2.2 Flip Angle Map Correction on Volume Coil

In previous work, coil sensitivity calculations were based on assuming a uniform B_1^- receiving magnetic field for the volume coil. In this work, the assumption of a uniform B_1^- in volume coil is loosened. In order to correct for the receive inhomogeneity of the volume coil, I instead assumed that the receive inhomogeneity factor $C_{B_1^-}^{VC}$ is equivalent to the transmit inhomogeneity factor $C_{B_1^+}^{VC}$. With this assumption $C_{B_1^-}^{VC} = C_{B_1^+}^{VC}$, the B_1^+ transmit inhomogeneity measured by DALL sequence can be used to correct for the B_1^- inhomogeneity.

This assumption is valid at magnetic fields of 3.0 T and below. However, in MRI, higher field strength is always desired for SNR consideration. However, at high field (7T and above), this assumption $C_{B_1^-}^{VC} = C_{B_1^+}^{VC}$ is no longer valid anymore(32). In order to get to compensate the B_1^- receiving field inhomogeneity of volume coil, a new method of accurate and rapid measurement of volume coil B_1^- receive field will be needed in order to implement absolute water and fat quantification at high field.

3.2.3 Temperature Correction

In the *in vivo* experiments I presented here, the temperature difference between human tissue and the phantom is not taken into account. Differences in temperature will lead to slight changes in the density of water in our reference phantom, thus confounding our

measurement. Although this effect did not appear to affect our results, it can be corrected by using an insulated reference with the same temperature as body tissue.

3.2.4 Cardiac Application

Many cardiac diseases are related to changing water or fat content. Imaging techniques has been investigated on myocardial edema, which is believed relevant to acute coronary syndromes (ACS) and myocardial infarction (49,50). Other possible applications of water fat separation techniques are found in characterizing cardiac masses, evaluating for myocardial lipomatous infiltration, and diagnosing pericarditis (51). Extending this absolute quantification technique to applications of cardiac imaging is promising.

In cardiac IDEAL imaging, one problem is that with low flip angles, is very difficult to get reasonable SNR in the volume coil reference image. This is partly because the cardiac experiments were only conducted for 2D imaging so far. Different from 3D experiment, 2D imaging experiment has only one shot per slice thus lack the extra SNR enhancement benefited from multiple shots z phased encoding. Methods to improve SNR in single slice cardiac volume coil image need to be investigated in the future.

To make the Double Angle Look-Locker (DALL) sequence transferable to cardiac applications, several issues need to be carefully considered and resolved. First, DALL is a 3D sequence, thus it takes longer to run comparing to the 2D single slice cardiac application. Parallel imaging might be used to speed up the data acquisition. Second is that the current version of DALL is not capable of ECG gating for cardiac imaging yet. The influence of motion artifacts prevents us from getting accurate measurement the B_1^+ transmitting magnetic field. The DALL sequence will need to be modified in the future in order to make it suitable for cardiac quantitative IDEAL measurement. Lowering

resolution of flip angle map might be helpful in reducing the effect of motion. Besides, motion artifact can be reduced by multiple identical acquisitions and then take the average of them.

3.2.5 Application in Hyperpolarized Imaging

In hyperpolarized imaging, nuclei such as ^{129}Xe or ^{13}C are used to label various low concentrations of compounds. Through the hyperpolarization process, signal can be dramatically enhanced up to tens of thousands of folds. The frequencies of ^{129}Xe or ^{13}C also change with different molecular environments in a manner similar to the proton resonance frequency change between water and fat. By applying the same algorithm as we used in water fat separation, least-squares chemical shift imaging (LSCSI) can be generalized to separate signals from different molecules in hyperpolarized ^{129}Xe or ^{13}C experiments. This will allow functional imaging of metabolism. For example, molecules like pyruvate can be labeled by ^{13}C . After injected into an animal, their frequency will change when a metabolic process converts the labeled molecule to a different metabolite.

The techniques developed in this thesis have the potential to be applicable to the absolute quantification of hyperpolarized species. Quantitative functional measurement of metabolism *in vivo* will provide an alternative powerful tool in physiological studies. The IDEAL method used for water and fat separation in this study (16), can be modified to monitor ^{13}C labeled pyruvate as it is metabolized to products such as lactate. These experiments are directly analogous to the water and fat separation performed with IDEAL in this study (16). Just like fat fraction is a biomarker in NAFLD diagnosis, lactate to pyruvate ratio is reported to be useful in diagnosing diseases like congenital lactic acidosis (40). Thus, chemical shift based absolute quantification techniques like the ones

reported in this thesis would be transferable to hyperpolarized ^{13}C imaging, and would allow absolute, rather than relative, quantification of metabolites.

3.3 Conclusion

In order to accurately measure the mass density of water and fat in abdomen, water and fat signals must be separated into water only and fat only images. Coil sensitivity inhomogeneity, flip angle inhomogeneity, and T_1 and T_2^* bias need to be corrected for in those images and then the corrected signal intensity must be calibrated to units of mass density. For abdominal imaging, which was the objective of this work, all of these corrections must be performed with measurements rapid enough to be acquired in a single 20 s breath hold. In this thesis, I corrected flip angle variations by measuring flip angle maps with the Double Angle Look-Locker sequence, which is the only flip angle measurement method fast enough to use in a breath hold. I corrected coil sensitivity variations by using a volume coil reference image, after correcting the volume coil images for flip angle variation. Small flip angles were used in data acquisition to minimize any T_1 bias. Finally, multi-peak T_2^* IDEAL acquisitions were used to separate fat from water and correct for T_2^* effects at the same time. The IDEAL acquisitions were accelerated with parallel MRI to allow acquisition of IDEAL data rapid enough to cover the entire liver in a single breath hold. I developed a method to combine all the necessary corrections and mass density calibration and demonstrated the feasibility of absolute quantification of water and fat mass density in abdomen.

References

1. Clark JM, Brancati FL, Diehl AM. Nonalcoholic fatty liver disease. *Gastroenterology* 2002;122(6):1649-1657.
2. Erickson SK. Nonalcoholic fatty liver disease. *Journal of lipid research* 2009;50 Suppl:S412-416.
3. Lazo M, Clark JM. The epidemiology of nonalcoholic fatty liver disease: a global perspective. *Seminars in liver disease* 2008;28(4):339-350.
4. Gower BA. Syndrome X in children: Influence of ethnicity and visceral fat. *Am J Hum Biol* 1999;11(2):249-257.
5. Jou J, Choi SS, Diehl AM. Mechanisms of disease progression in nonalcoholic fatty liver disease. *Seminars in liver disease* 2008;28(4):370-379.
6. Dienstag JL. The role of liver biopsy in chronic hepatitis C. *Hepatology* 2002;36(5 Suppl 1):S152-160.
7. Bravo AA, Sheth SG, Chopra S. Liver biopsy. *The New England journal of medicine* 2001;344(7):495-500.
8. Ma J, Wehrli FW, Song HK, Hwang SN. A single-scan imaging technique for measurement of the relative concentrations of fat and water protons and their transverse relaxation times. *J Magn Reson* 1997;125(1):92-101.
9. Meisamy S, Hines CD, Hamilton G, Sirlin CB, McKenzie CA, Yu H, Brittain JH, Reeder SB. Quantification of hepatic steatosis with T1-independent, T2-corrected MR imaging with spectral modeling of fat: blinded comparison with MR spectroscopy. *Radiology* 2011;258(3):767-775.
10. Szczepaniak LS, Nurenberg P, Leonard D, Browning JD, Reingold JS, Grundy S, Hobbs HH, Dobbins RL. Magnetic resonance spectroscopy to measure hepatic triglyceride content: prevalence of hepatic steatosis in the general population. *American journal of physiology Endocrinology and metabolism* 2005;288(2):E462-468.

11. Dixon WT. Simple proton spectroscopic imaging. *Radiology* 1984;153(1):189-194.
12. Glover GH, Schneider E. Three-point Dixon technique for true water/fat decomposition with B₀ inhomogeneity correction. *Magnetic resonance in medicine : official journal of the Society of Magnetic Resonance in Medicine / Society of Magnetic Resonance in Medicine* 1991;18(2):371-383.
13. Yu H, Shimakawa A, McKenzie CA, Brodsky E, Brittain JH, Reeder SB. Multiecho water-fat separation and simultaneous R₂* estimation with multifrequency fat spectrum modeling. *Magnetic resonance in medicine : official journal of the Society of Magnetic Resonance in Medicine / Society of Magnetic Resonance in Medicine* 2008;60(5):1122-1134.
14. Yu H, McKenzie CA, Shimakawa A, Vu AT, Brau AC, Beatty PJ, Pineda AR, Brittain JH, Reeder SB. Multiecho reconstruction for simultaneous water-fat decomposition and T₂* estimation. *Journal of magnetic resonance imaging : JMRI* 2007;26(4):1153-1161.
15. Thomsen C, Becker U, Winkler K, Christoffersen P, Jensen M, Henriksen O. Quantification of liver fat using magnetic resonance spectroscopy. *Magnetic Resonance Imaging* 1994;12(3):487-495.
16. Reeder SB, Pineda AR, Wen Z, Shimakawa A, Yu H, Brittain JH, Gold GE, Beaulieu CH, Pelc NJ. Iterative decomposition of water and fat with echo asymmetry and least-squares estimation (IDEAL): application with fast spin-echo imaging. *Magnetic resonance in medicine : official journal of the Society of Magnetic Resonance in Medicine / Society of Magnetic Resonance in Medicine* 2005;54(3):636-644.
17. Reeder SB, Wen Z, Yu H, Pineda AR, Gold GE, Markl M, Pelc NJ. Multicoil Dixon chemical species separation with an iterative least-squares estimation method. *Magnetic resonance in medicine : official journal of the Society of Magnetic Resonance in Medicine / Society of Magnetic Resonance in Medicine* 2004;51(1):35-45.
18. Szczepaniak LS, Babcock EE, Schick F, Dobbins RL, Garg A, Burns DK, McGarry JD, Stein DT. Measurement of intracellular triglyceride stores by H

- spectroscopy: validation in vivo. *The American journal of physiology* 1999;276(5 Pt 1):E977-989.
19. Axel L, Hayes C. Surface coil magnetic resonance imaging. *Archives internationales de physiologie et de biochimie* 1985;93(5):11-18.
 20. Axel L. Surface coil magnetic resonance imaging. *Journal of computer assisted tomography* 1984;8(3):381-384.
 21. Roemer PB, Edelstein WA, Hayes CE, Souza SP, Mueller OM. The NMR phased array. *Magnetic Resonance in Medicine* 1990;16(2):192-225.
 22. Jin J, Liu F, Weber E, Li Y, Crozier S. An electromagnetic reverse method of coil sensitivity mapping for parallel MRI - theoretical framework. *J Magn Reson* 2010;207(1):59-68.
 23. Murakami JW, Hayes CE, Weinberger E. Intensity correction of phased-array surface coil images. *Magnetic resonance in medicine : official journal of the Society of Magnetic Resonance in Medicine / Society of Magnetic Resonance in Medicine* 1996;35(4):585-590.
 24. Vemuri P, Kholmovski EG, Parker DL, Chapman BE. Coil sensitivity estimation for optimal SNR reconstruction and intensity inhomogeneity correction in phased array MR imaging. *Information processing in medical imaging : proceedings of the conference* 2005;19:603-614.
 25. Brey WW, Narayana PA. Correction for intensity falloff in surface coil magnetic resonance imaging. *Medical physics* 1988;15(2):241-245.
 26. Van de Moortele PF, Akgun C, Adriany G, Moeller S, Ritter J, Collins CM, Smith MB, Vaughan JT, Ugurbil K. B(1) destructive interferences and spatial phase patterns at 7 T with a head transceiver array coil. *Magn Reson Med* 2005;54(6):1503-1518.
 27. Stollberger R, Wach P. Imaging of the active B1 field in vivo. *Magn Reson Med* 1996;35(2):246-251.
 28. Wade T, McKenzie C, Rutt B. No Inversion Double Angle Look-Locker (NiDALL) for Flip Angle. 2010.

29. Look DC. Time Saving in Measurement of NMR and EPR Relaxation Times. *Review of Scientific Instruments* 1970;41(2):250.
30. Henderson E, McKinnon G, Lee TY, Rutt BK. A fast 3D look-locker method for volumetric T1 mapping. *Magn Reson Imaging* 1999;17(8):1163-1171.
31. Cortez-Pinto H, Camilo ME, Baptista A, De Oliveira AG, De Moura MC. Non-alcoholic fatty liver: another feature of the metabolic syndrome? *Clin Nutr* 1999;18(6):353-358.
32. van den Bergen B, Van den Berg CA, Bartels LW, Lagendijk JJ. 7 T body MRI: B1 shimming with simultaneous SAR reduction. *Physics in medicine and biology* 2007;52(17):5429-5441.
33. Neeb H, Zilles K, Shah NJ. A new method for fast quantitative mapping of absolute water content in vivo. *Neuroimage* 2006;31(3):1156-1168.
34. Neeb H, Ermer V, Stocker T, Shah NJ. Fast quantitative mapping of absolute water content with full brain coverage. *Neuroimage* 2008;42(3):1094-1109.
35. Hu HH, Nayak KS. Quantification of absolute fat mass using an adipose tissue reference signal model. *Journal of magnetic resonance imaging : JMRI* 2008;28(6):1483-1491.
36. Liu CY, McKenzie CA, Yu H, Brittain JH, Reeder SB. Fat quantification with IDEAL gradient echo imaging: correction of bias from T(1) and noise. *Magnetic resonance in medicine : official journal of the Society of Magnetic Resonance in Medicine / Society of Magnetic Resonance in Medicine* 2007;58(2):354-364.
37. Pruessmann KP, Weiger M, Scheidegger MB, Boesiger P. SENSE: sensitivity encoding for fast MRI. *Magnetic resonance in medicine : official journal of the Society of Magnetic Resonance in Medicine / Society of Magnetic Resonance in Medicine* 1999;42(5):952-962.
38. Hines CDG, Yu H, Shimakawa A, McKenzie CA, Brittain JH, Reeder SB. T1 independent, T2* corrected MRI with accurate spectral modeling for quantification of fat: Validation in a fat-water-SPIO phantom. *Journal of Magnetic Resonance Imaging* 2009;30(5):1215-1222.

39. Lipicky RJ, Bryant SH, Salmon JH. Cable parameters, sodium, potassium, chloride, and water content, and potassium efflux in isolated external intercostal muscle of normal volunteers and patients with myotonia congenita. *J Clin Invest* 1971;50(10):2091-2103.
40. Forbes RM, Cooper AR, Mitchell HH. The composition of the adult human body as determined by chemical analysis. *The Journal of biological chemistry* 1953;203(1):359-366.
41. Yang IY, Cui Y, Wiens CN, Wade TP, McKenzie CA. Fat Fraction Bias Correction using T1 estimates and Flip Angle Mapping. 2012; Melbourne, Australia.
42. Hahn EL. An Accurate Nuclear Magnetic Resonance Method for Measuring Spin-Lattice Relaxation Times. *Physical Review* 1949;76(1):145-146.
43. Li X, Han ET, Busse RF, Majumdar S. In vivo T(1rho) mapping in cartilage using 3D magnetization-prepared angle-modulated partitioned k-space spoiled gradient echo snapshots (3D MAPSS). *Magnetic resonance in medicine : official journal of the Society of Magnetic Resonance in Medicine / Society of Magnetic Resonance in Medicine* 2008;59(2):298-307.
44. Dall'Armellina E, Piechnik SK, Ferreira VM, Si QL, Robson MD, Francis JM, Cuculi F, Kharbanda RK, Banning AP, Choudhury RP, Karamitsos TD, Neubauer S. Cardiovascular magnetic resonance by non contrast T1-mapping allows assessment of severity of injury in acute myocardial infarction. *Journal of cardiovascular magnetic resonance : official journal of the Society for Cardiovascular Magnetic Resonance* 2012;14:15.
45. Barral JK, Gudmundson E, Stikov N, Etezadi-Amoli M, Stoica P, Nishimura DG. A robust methodology for in vivo T1 mapping. *Magnetic resonance in medicine : official journal of the Society of Magnetic Resonance in Medicine / Society of Magnetic Resonance in Medicine* 2010;64(4):1057-1067.
46. Deoni SC, Peters TM, Rutt BK. High-resolution T1 and T2 mapping of the brain in a clinically acceptable time with DESPOT1 and DESPOT2. *Magnetic resonance in medicine : official journal of the Society of Magnetic Resonance in Medicine / Society of Magnetic Resonance in Medicine* 2005;53(1):237-241.

47. Deoni SC, Rutt BK, Peters TM. Rapid combined T1 and T2 mapping using gradient recalled acquisition in the steady state. *Magnetic resonance in medicine : official journal of the Society of Magnetic Resonance in Medicine / Society of Magnetic Resonance in Medicine* 2003;49(3):515-526.
48. Look DC, Locker DR. Time Saving in Measurement of NMR and EPR Relaxation Times. *The Review of Scientific Instruments* 1970;41(2):250-251.
49. Walls MC, Verhaert D, Min JK, Raman SV. Myocardial edema imaging in acute coronary syndromes. *Journal of magnetic resonance imaging : JMRI* 2011;34(6):1243-1250.
50. Abdel-Aty H. Myocardial edema imaging of the area at risk in acute myocardial infarction: seeing through water. *JACC Cardiovascular imaging* 2009;2(7):832-834.
51. Farrelly C, Shah S, Davarpanah A, Keeling AN, Carr JC. ECG-gated multiecho Dixon fat-water separation in cardiac MRI: advantages over conventional fat-saturated imaging. *AJR American journal of roentgenology* 2012;199(1):W74-83.

Curriculum Vitae

Name: Yifan Cui

Post-secondary Education and Degrees: Nankai University
Tianjin, P. R. China
2006-2010 B.Sc.

The University of Western Ontario
London, Ontario, Canada
2010-2012 M.Sc. candidate

Honours and Awards: **Summa Cum Laude Merit Award**
International Society of Magnetic Resonance Imaging in Medicine (ISMRM) annual conference 2012, Melbourne, Australia

University Scholarship (Nankai University)
2007-2008, 2009-2010

National Encouragement Scholarship
2008-2009

Social Science and Humanities Research Council (SSHRC)
Doctoral Fellowship
1995-1999

Related Work Experience

Teaching Assistant
The University of Western Ontario
2010-2012

Research Assistant
The University of Western Ontario
2010-2012

Publications:

Yifan Cui, Issac Y. Yang, Trevor P. Wade, Curtis N. Wiens, Abraam S. Soliman, and Charles A. McKenzie

Absolute Quantification of *In Vivo* Water and Fat Content

ISMRM 2012 (oral presentation)

Issac Y. Yang, Yifan Cui, Curtis N. Wiens, Trevor P. Wade, and Charles A. McKenzie

Fat Fraction Bias Correction using T1 estimates and Flip Angle Mapping

ISMRM 2012 (poster presentation)

Yifan Cui, Issac Y. Yang, Trevor P. Wade, Curtis N. Wiens, Abraam S. Soliman, and Charles A. McKenzie

Absolute Quantification Of In Vivo Water & Fat Content

ISMRM Scientific workshop---Fat-Water Separation 2012 (poster presentation)

Issac Y. Yang, Yifan Cui, Curtis N. Wiens, Trevor P. Wade, and Charles A. McKenzie

Fat Fraction Bias Correction using T1 estimates & Rapid 3D Flip Angle Mapping

ISMRM Scientific workshop---Fat-Water Separation 2012 (poster presentation)